Electronic Supplementary Information

Oxygen-Coordinated Cobalt Single-Atom Electrocatalyst Boosting Urea and Urea Peroxide Production

Shengbo Zhang,[†ab] Meng Jin,[†ab] Hui Xu,[†ab] Xinyuan Zhang,[ab] Tongfei Shi,[*ab] Yixing Ye,[ab] Yue Lin,[c] Lirong Zheng,[d] Guozhong Wang,[ab] Yunxia Zhang,[ab] Huajie Yin,[ab] Haimin Zhang,[*ab] and Huijun Zhao[e]

a. *Key Laboratory of Materials Physics, Centre for Environmental and Energy Nanomaterials, Anhui Key Laboratory of Nanomaterials and Nanotechnology, CAS Center for Excellence in Nanoscience, Institute of Solid State Physics, Chinese Academy of Sciences, Hefei 230031, China. E-mail:* zhanghm@issp.ac.cn, tfshi@issp.ac.cn

b. *University of Science and Technology of China, Hefei 230026, China*

c. *Hefei National Research Center for Physical Sciences at the Microscale, University of Science and Technology of China, Hefei 230026, PR China*

d. *Beijing Synchrotron Radiation Facility, Institute of High Energy Physics, Chinese Academy of Sciences, 19B Yuquan Road, Beijing 100049, PR China*

e. *Center for Catalysis and Clean Energy, Griffith University, Gold Coast Campus, QLD4222, Australia*

† *These authors contributed equally to this work*

Experimental Section

Methods

Reagents and materials. Bacterial cellulose (BC) pellicle was obtained from Guilin Qihong Technology Co., Ltd., China. $Co(NO_3)\cdot6H_2O$ were purchased from Sinopharm Chemical Reagent Co., Ltd. $HKCO_3$ (99.5%), KNO_3 (99.0%), sodium nitroferricyanide(III) dehydrate ($C_5FeN_6Na_2O\cdot2H_2O$, 99.0%), sodium citrate ($C_6H_5Na_3O_7\cdot2H_2O$, 99.0%), NaOH (96.0%), salicylic acid ($C_7H_6O_3$, 99.5%), NaClO (available chlorine $\geq$ 5.0%), NH_4Cl (99.5%), H_3PO_4 ($\geq$ 85%), H_2SO_4 ($\geq$ 85%), *p*-aminobenzenesuifonamide ($NH_2C_6H_4SO_2NH_2$, 95.0%), N-(1-naphthyl) ethylenediamine dihydrochloride ($C_{10}H_7NHC_2H_4NH_2\cdot2HCl$, 95.0%), $^{15}KNO_3$ (AR), $^{14}NH_2CO^{14}NH_2$ (AR), $^{15}NH_2CO^{15}NH_2$ (AR), CoPc and CoO references were purchased from Shanghai Aladdin Biochemical Technology Co., Ltd. All solutions were prepared using deionized water (Millipore Corp., 18.2 MΩ cm). Commercial carbon paper (CP, HCP030N) was purchased from Shanghai Hesen Electric Co. Ltd.

Fabrication of Co-NPs/CBC, Co-O-C and CBC. BC pellicle was frozen by liquid nitrogen and freeze-dried in a bulk tray dryer at a sublimating temperature of -75 °C and a pressure of 0.01 m bar for 48 h. The pre-treated BC was used as the adsorbent to controllably impregnate Co^{2+}. The BC (1.0 g) was immersed in a 400 mL solution containing 48 mmol of $Co(NO_3)\cdot6H_2O$ (Concentration of Co^{2+}: 120 mmol L^{-1}) for 6 h. The BC with adsorbed Co^{2+} was adequately washed with deionized water, freeze-dried and subjected to the pyrolytic treatment at 360 °C for 2 h then 700 °C for 3 h under Ar atmosphere to carbothermally reduce the adsorbed Co^{2+} on BC to metallic Co NPs and simultaneously carbonise BC into graphitic carbon (CBC). The resultant Co-NPs/CBC was adequately washed with deionised water and ethanol, dried at 60 °C under vacuum for 6 h, followed by a refluxing acid-etching process using 2.0 M H_2SO_4 at 120 °C for 6 h to remove metallic Co NPs. The resultant Co-O-C was adequately washed with distilled water and ethanol, and dried under vacuum for 12 h. The CBC sample without Co was fabricated by the pyrolytic treatment of BC precursor at 360 °C for 2 h then 700 °C for 2 h under Ar atmosphere.

Characterization. XRD patterns were acquired using Philips X'pert PRO with Nifiltered

monochromatic CuKa radiation (λKα1=1.5418 Å) at 40 kV and 40 mA. FT-IR spectra were measured by a Nicolet Nexus FT-IR spectrometer with KBr pellet technique ranging from 400 to 4000 cm^{-1} at room temperature. SEM images were obtained using SU8020 (Hitachi, Japan) with a field emission scanning electron microanalyzer at an acceleration voltage of 10.0 kV. TEM images were obtained using JEMARM 200F operating at an accelerating voltage of 200 kV. XPS measurements were performed on an ESCALAB 250 X-ray photoelectron spectrometer (Thermo, America) equipped with Al Kα1, 2 monochromatized radiations at 1486.6 eV X ray source. The Pd and Cu contents were quantitatively determined by the ICP-AES (ICP-6300, Thermo Fisher Scientific). Nitrogen adsorption-desorption isotherms were measured using an automated gas sorption analyzer (Autosorb-iQ-Cx). The synchrotron-based X-ray X-ray absorption near-edge structure (XANES) and the extended X-ray absorption fine structure (EXAFS) measurements were performed at the 1W1B station of Beijing Synchrotron Radiation Facility, China. The EXAFS data were processed according to the standard procedures using the ATHENA module implemented in the IFEFFIT software packages. Co^{2+} and metallic Co contents were quantitatively determined by ICP-AES (ICP-6300, Thermo Fisher Scientific).

Operando ATR-SERIES measurements. The *operando* attenuated total reflection surface-enhanced infrared adsorption spectroscopy (ATR-SEIRAS) was performed on a FTIR spectrometer (Nicolet iS50, Thermo Scientific) equipped with an MCT-A detector with silicon as the prismatic window. Fist, Co-O-C ink (pure ethanol as a dispersant) was carefully dropped on the surface of gold film, which was chemically deposited on the surface of the silicon prismatic before each experiment. Then the deposited silicon prismatic served as the working electrode. The platinum mesh and Ag/AgCl electrode containing saturated KCl solution were used as the counter and reference electrodes, respectively. The CO_2-saturated 0.1 M $KHCO_3$ + 0.05 M KNO_3 solution was employed as the electrolyte. Each infrared absorption spectrum was acquired by averaging 128 scans at a resolution of 4.0 cm^{-1}. The background spectrum of the catalyst electrode was acquired at an open-circuit voltage before each systemic measurement, and the measured potential ranges of the electrocatalysis were −1.0 to −1.6 V *vs.* RHE with an interval of 0.1 V.

Operando Raman measurements. For the *operando* Raman tests, the samples were recorded on a RXN1-785 Raman spectrometer (Analytik Jena AG, excited wavelength of 785 nm) connected with CHI 660 E electrochemical workstation.

Electrochemical measurements. All electrochemical measurements were performed on a CHI 660E electrochemical workstation (CH Instrumental Corporation, Shanghai, China) under ambient conditions using a Nafion 211 proton exchange membrane separated two-compartment H-type electrochemical cell accommodated 50 mL of CO_2-saturated 0.1 M $KHCO_3$ + 0.05 M KNO_3 electrolyte in each compartment and a three-electrode electrochemical system with a Co-O-C working electrode, an Ag/AgCl (Saturated KCl) reference electrode and a Pt mesh counter electrode. Prior to use, the Nafion 211 membrane was treated by successive heating at 80 °C in H_2O_2 (5.0 wt.%) aqueous solution for 1 h and in deionized water for another 1 h. The working electrode was prepared as follows: 2.5 mg of the targeted electrocatalyst was firstly dispersed in 95 µL of absolute ethanol and 5.0 µL of Nafion solution (5.0 wt.%) under sonication for 30 min to form a homogeneous ink. 10 µL of ink was loaded onto carbon paper electrode (1×1 cm^2, equivalent to 0.25 mg cm^{-2}) and dried under ambient conditions for 40 min before use. Before the electrocatalysis, Ar gas was persistently bubbled into the electrolyte to eliminate O_2 interference and the electrolyte was bubbled with CO_2 for 20 min. Then the purified CO_2 was continuously fed into the cathodic compartment with a constant flow rate of 20 mL min^{-1} during the experiments. The electrolyte in the cathodic compartment was stirred at a rate of 500 rpm during electrocatalysis. In this work, all measured potentials *vs.* Ag/AgCl were converted to the potentials *vs.* RHE (E_{RHE}) according to the following equation:

$$E_{RHE} = E_{Ag/AgCl} + 0.059pH + E^{\circ}{}_{Ag/AgCl}$$

(1)

where, $E_{Ag/AgCl}$ is the equilibrium potential under standard conditions, $E^{\circ}{}_{Ag/AgCl} = 0.1967$ V *vs.* RHE at 25 °C.

Determination of urea, ammonia, nitrite and hydrazine. As-produced urea was determined by the urease decomposition and ^1H NMR method.[1-2] The content of nitrite in the electrolyte

was also measured by ultraviolet spectrophotometry.[1-2] The yielded ammonia was determined by the standard indophenol blue method.[1-2]

Isotope labelling experiments. For quality assurance required, ^{15}N isotopic labelling experiments were conducted using CO_2-saturated 0.1 M $KHCO_3$ + 0.05 M $K^{15}NO_3$ as the electrolyte with identical experimental procedure as that of CO_2-saturated 0.05 M $K^{14}NO_3$ experiments. The yielded $^{15}NH_2CO^{15}NH_2$ and $^{14}NH_2CO^{14}NH_2$ were analyzed by the ^{1}H NMR and ^{15}N NMR methods using Bruker Avance-600 MHZ.

Calculation of R_{urea}, R_{NH3}, R_{NO2}^- and FE. R_{urea} and FE are calculated by the following equations:

$$R_{urea} (\mu g\ h^{-1}\ mg_{cat.}^{-1}) = \frac{C_{urea}(\mu g\ mL^{-1}) \times V(mL)}{t\,(h) \times m_{cat.}\,(mg)} \tag{2}$$

$$FE\,(\%) = \frac{16 \times n_{urea}\,(mol) \times F\,(C\ mol^{-1})}{Q\,(C)} \times 100\% \tag{3}$$

where, C_{urea} and V are the measured urea concentration and the electrolyte solution volume, respectively, t is the electrolysis period and $m_{cat.}$ is the amount of the loaded electrocatalyst, F is the faradaic constant (96485 C mol^{-1}) and Q is the total charge transferred during electrolysis period.

R_{NH3} and FE are calculated by the following equations:

$$R_{NH3} (\mu g\ h^{-1}\ mg_{cat.}^{-1}) = \frac{C_{NH3}(\mu g\ mL^{-1}) \times V(mL)}{t\,(h) \times m_{cat.}\,(mg)} \tag{4}$$

$$FE\,(\%) = \frac{8 \times n_{NH3}\,(mol) \times F\,(C\ mol^{-1})}{Q\,(C)} \times 100\% \tag{5}$$

where, C_{NH3} and V are the measured NH_3 concentration and the electrolyte solution volume, respectively, t is the electrolysis period and $m_{cat.}$ is the amount of the loaded electrocatalyst, F is the faradaic constant (96485 C mol^{-1}) and Q is the total charge transferred during electrolysis period.

R_{NO2}^- and FE are calculated by the following equations:

$$R_{NO_2^-} (\mu g \ h^{-1} \ mg_{cat.}^{-1}) = \frac{C_{NO_2^-} (\mu g \ mL^{-1}) \times V (mL)}{t \ (h) \times m_{cat.} \ (mg)} \tag{6}$$

$$FE \ (\%) = \frac{2 \times n_{NO_2^-} (mol) \times F \ (C \ mol^{-1})}{Q \ (C)} \times 100\% \tag{7}$$

where, $C_{NO_2^-}$ and V are the measured NO_2^- concentration and the electrolyte solution volume, respectively, t is the electrolysis period and $m_{cat.}$ is the amount of the loaded electrocatalyst, F is the faradaic constant (96485 C mol^{-1}) and Q is the total charge transferred during electrolysis period.

Determination of carbon monoxide (CO) and hydrogen (H₂). The amounts of CO and H$_2$ were quantitatively analyzed by gas chromatography (GC) measurements.

Calculation of H₂O₂ concentration. The H$_2$O$_2$ concentration in the electrolyte was quantified by ceric sulfate titration following the reaction:

$$2Ce^{4+} + H_2O_2 \rightarrow 2Ce^{3+} + 2H^+ + O_2$$
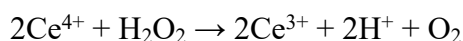
where, the yellow-colored Ce^{4+} was reduced by H_2O_2 to colorless Ce^{3+} and can be measured by ultraviolet-visible spectroscopy. A series of standard $Ce(SO_4)_2$ solution was prepared by dissolving $Ce(SO_4)_2$ in 0.5 M H_2SO_4, then we obtained the calibration curves between the absorbance and concentration of Ce^{4+} performed on spectrophotometer at 317 nm. Thus, the concentration of H_2O_2 can be calculated based on the absorbance before and after reaction.

Calculation of H₂O₂ FE. The FE of H_2O_2 was calculated by the following equation:

$$FE \ (\%) = \frac{2 \times n_{H_2O_2} (mol) \times F \ (C \ mol^{-1})}{Q \ (C)} \times 100\% \tag{8}$$

where, F is the Faradaic constant (96485 C mol^{-1}) and Q is the total charge transferred during the electrocatalysis period.

Theoretical calculations. All the spin-polarized DFT calculations were performed using the Vienna Ab-initio Simulation Package (VASP), and the generalized gradient approximation (GGA) with the Perdew-Burke-Ernzerhof (PBE) exchange-correlation functional was used with the projector augmented wave method. A kinetic energy cutoff of 450 eV was used for

plane wave expansion, the convergence threshold was set as 10^{-5} eV in energy and 0.02 eV

$Å^{-1}$ in force. The vacuum distance was set to 15 Å to minimize the artificial interactions of

the interlayer.[3-4] During the total calculations, the symmetry was switched off and the dipolar

correction was also included. DFT-D3 method was used for the dispersion correction.[5] The

Gibbs free energy of the NRR reaction pathways was referenced to the computational

hydrogen electrode (CHE) model, which proposed by Nørskov and co-workers.[6]

Supplementary Tables and Figures

Table S1. Structural parameters extracted from the Co *K*-edge EXAFS fitting data of Co-O-C before and under various potentials during C−N coupling.

Samples	Scattering Pair	CN	R (Å)	$\sigma^2(10^{-3}Å^2)$	$\mathit{\Delta}E_0$ (eV)
Co foil	Co-Co	12.00	2.49	6.17	6.74
Co-NPs/CBC	Co-Co	8.50	2.50	6.56	7.25
Co-O-C (As synthesised)	Co-O	4.00	1.97	8.91	5.61
Co-O-C (-1.1 V)	Co-O	4.60	2.07	4.98	-0.89
Co-O-C (-1.3 V)	Co-O	4.65	2.09	4.60	-0.90
Co-O-C (-1.5 V)	Co-O	4.70	2.08	4.46	-1.34
Co-O-C (OCP)	Co-O	4.00	1.98	9.48	8.82

CN is the coordination number; R is interatomic distance (the bond length between central atoms and surrounding coordination atoms); σ^2 is Debye-Waller factor (a measure of thermal and static disorder); $\mathit{\Delta}E_0$ is edge-energy shift (the difference between the zero kinetic energy value of the sample and that of the theoretical model).

Table S2. Electrocatalytic urea synthesis performance of the reported elecatalysts and Co-O-C.

Ref	Catalyst	Reactant	Conditions	Urea Production Rate	FE (%)	By-product
7	Pd_1Cu_1/TiO_2-400	$N_2 + CO_2$	0.1 M $KHCO_3$	3.36 mmol h^{-1} g^{-1}	8.92	CO, H_2, NH_3
8	PPy-coated Pt	$N_2 + CO_2$	0.1 M Li_2SO_4/ 0.03 M H^+	2.4 μmol h^{-1}	7.1	NH_3, $HCOOH$
9	$Bi/BiVO_4$	$N_2 + CO_2$	0.1 M $KHCO_3$	5.91 mmol h^{-1} g^{-1}	12.55	CO, H_2, NH_3
10	$BiFeO_3/BiVO_4$	$N_2 + CO_2$	0.1 M $KHCO_3$	4.94 mmol h^{-1} g^{-1}	17.18	CO, H_2, NH_3
11	$Ni_3(BO_3)_2$	$N_2 + CO_2$	0.1 M $KHCO_3$	9.70 mmol h^{-1} g^{-1}	20.36	CO, H_2, NH_3
12	Co-PMDA-2-mbIM	$N_2 + CO_2$	0.1 M $KHCO_3$	14.47 mmol h^{-1} g^{-1}	48.97	CO, H_2, NH_3
13	Rice-like InOOH	$N_2 + CO_2$	0.1 M $KHCO_3$	6.85 mmol h^{-1} g^{-1}	20.97	CO, H_2, NH_3
14	Pd_1Cu_1-TiO_2	$N_2 + CO_2$	0.5 M K_2SO_4	166.67 mol h^{-1} mol_{Pd}^{-1}	22.54	H_2, NH_3
15	Zn-Mn/N, Cl	$N_2 + CO_2$	1.0 M H_2SO_4	4.13 mmol h^{-1} g^{-1}	63.5	CO, H_2, NH_3
16	V_N-Cu_3N-300	$N_2 + CO_2$	0.1 M $KHCO_3$	81 μg cm^{-2} h^{-1}	28.7	CO, H_2, NH_3
17	$Sb_xBi_{1-x}O_y$	$N_2 + CO_2$	0.5 M K_2SO_4	307.97 μg h^{-1} $mg_{cat.}^{-1}$	10.9	CO, H_2, $HCOOH$, NH_3
18	MoP	$N_2 + CO_2$	0.1 M K_2SO_4	12.4 μg h^{-1} $mg_{cat.}^{-1}$	36.5	H_2, NH_3
19	Ni-Pc	$NO_2^- + CO_2$	0.2 M $KHCO_3$	-	40	CO, NH_3
20	$FeTiO_3$	$NO_2^- + CO_2$	1.0 M $NaHCO_3$	-	-	-
21	Cu-TiO_2	$NO_2^- + CO_2$	0.2 M $KHCO_3$	20 μmol h^{-1}	43.1	CO, H_2, N_2, NH_3
22	Te-Pd NCs	$NO_2^- + CO_2$	0.05 M KNO_2	-	12.2	CO, H_2, N_2, NH_3

23	AuCu SANFs	$NO_2^- + CO_2$	0.01 M KNO$_2$	3889.6 μg h^{-1} mg$_{cat.}^{-1}$	24.7	CO, H$_2$, N$_2$, NH$_3$
24	ZnO-V	$NO_2^- + CO_2$	0.2 M NaHCO$_3$ + 0.1 M NaNO$_2$	16.56 μmol h^{-1}	23.26	CO, H$_2$, NO, NH$_3$
25	Co–NiO$_x$@ GDY	$NO_2^- + CO_2$	0.01 M NaNO$_2$	913.2 μg h^{-1} mg$_{cat.}^{-1}$	64.3	CO, H$_2$, N$_2$, NH$_3$,
26	Zn nanobelts	$NO + CO_2$	0.2 M KHCO$_3$	15.13 mmol h^{-1} g^{-1}	11.26	CO, H$_2$, NH$_3$
27	Cu-loaded gas-diffusion electrode	$NO_2^- + CO_2$	0.2 M KHCO$_3$	-	10	CO, HCOOH, NH$_3$
		$NO_3^- + CO_2$	0.2 M KHCO$_3$	-	35	
28	TiO$_2$-Nafion	$NO_3^- + CO_2$	0.1 M KNO$_3$	0.33 μmol h^{-1}	40	CO, H$_2$, NH$_3$
29	Vo-InOOH	$NO_3^- + CO_2$	0.1 M KNO$_3$	592.5 μg h^{-1} mg$_{cat.}^{-1}$	51.0	CO, H$_2$, NH$_3$
30	In(OH)$_3$-S	$NO_3^- + CO_2$	0.1 M KNO$_3$	533.1 μg h^{-1} mg$_{cat.}^{-1}$	53.4	CO, H$_2$, NH$_3$
31	Cu@Zn	$NO_3^- + CO_2$	0.1 M KNO$_3$ + 0.2 M KHCO$_3$	7.29 μmol cm^{-2} h^{-1}	9.28	N$_2$, CO, H$_2$, NH$_3$, NO$_2^-$
1	Vo-CeO$_2$-750	$NO_3^- + CO_2$	0.1 M KHCO$_3$ + 50m M KNO$_3$	943.6 μg h^{-1} mg$_{cat.}^{-1}$	-	CO, H$_2$, NH$_3$, NO$_2^-$
2	PdCu/CBC	$NO_3^- + CO_2$	0.05 M KNO$_3$	763.8 ± 42.8 μg h^{-1} mg$_{cat.}^{-1}$	69.1 ± 3.8	CO, H$_2$, NO$_2^-$, NH$_3$
32	Cu-GS-800	$NO_3^- + CO_2$	0.1 M K$_2$SO$_4$ + 0.1 M KNO$_3$	1800 μg h^{-1} mg$_{cat.}^{-1}$	28	CO, H$_2$, NH$_3$
33	F-CNT-300	$NO_3^- + CO_2$	0.1 M KNO$_3$	6.36 mmol h^{-1} g$_{cat.}^{-1}$	18.0	H$_2$, NH$_3$
34	Ru-Cu CF	$NO_3^- + CO_2$	0.1 M NaNO$_3$	151.6 μg h^{-1} cm^{-2}	25.4	CO, H$_2$, HCOOH ,

						NO_2^-, NH_3
35	B-FeNi-DASC	$NO_3^- + CO_2$	0.1 M KHCO$_3$ + 50m M KNO$_3$	20.2 mmol h^{-1} g$_{cat.}^{-1}$	17.8	CO, H$_2$, NH$_3$
36	Fe(a)@C-Fe$_3$O$_4$/CNT	$NO_3^- + CO_2$	0.1 M KNO$_3$	1341.0 ± 112.6 μg h^{-1} mg$_{cat.}^{-1}$	16.5 ± 6.1	CO, H$_2$, NO_2^-, NH$_3$
37	Cu$_1$-CeO$_2$	$NO_3^- + CO_2$	0.1 M KHCO$_3$ + 0.05 M KNO$_3$	52.84 mmol h^{-1} g$_{cat.}^{-1}$	-	CO, H$_2$, C$_2$H$_4$, CH$_4$, NO_2^-, NH$_3$
38	CoPc-COF	$NO_3^- + CO_2$	0.3 M KHCO$_3$ + 0.2 M KNO$_3$	1205 μg h^{-1} cm^{-2}	49.0	CO, H$_2$, NO_2^-, NH$_3$
39	Cu-SP-OMe	$NO_3^- + CO_2$	0.1 M KHCO$_3$ + 0.01 M KNO$_3$	3640 μg h^{-1} mg$_{cat.}^{-1}$	57.9 ± 3	NO_2^-, NH$_3$
40	Cu$_{97}$In$_3$-C	$NO_3^- + CO_2$	0.1 M KHCO$_3$ + 0.01 M KNO$_3$	13.1 mmol h^{-1} g$_{cat.}^{-1}$	-	-
41	MoO$_x$/C	$NO_3^- + CO_2$	0.1 M KNO$_3$	1341.5 μg h^{-1} mg$_{cat.}^{-1}$	27.7	CO, H$_2$, NO_2^-, NH$_3$
42	m-Cu$_2$O	$NO_3^- + CO_2$	0.1 M KHCO$_3$ + 0.01 M KNO$_3$	29.2 mmol h^{-1} g$_{cat.}^{-1}$	-	-
		$NO_2^- + CO_2$	0.1 M KHCO$_3$ + 0.01 M KNO$_2$	114.0 mmol h^{-1} g$_{cat.}^{-1}$	-	-
43	6Å-Cu	$NO_3^- + CO_2$	1.0 M KOH + 0.1 M KNO$_3$	7541.9 μg h^{-1} mg$_{cat.}^{-1}$	51.97 ± 0.8	CO, H$_2$, C$_2$H$_4$, HCONH$_2$, CH$_3$CONH$_2$
44	Cu$_{1.0}$/ZnO$_{0.5}$ GDE	$NO_3^- + CO_2$	0.1 M KHCO$_3$ +	3.2 μmol h^{-1} cm^{-2}	37.4	-

			0.1 M KNO$_3$			
45	CuWO$_4$	NO$_3^-$ + CO$_2$	0.1 M KNO$_3$	98.5 ± 3.2 μg h^{-1} mg$_{cat.}$$^{-1}$	70.1 ± 2.4	CO, H$_2$, NO$_2^-$, NH$_3$
46	N-C-1000	NO$_3^-$ + CO$_2$	0.1 M KHCO$_3$ + 0.1 M KNO$_3$	498.5 μg h^{-1} mg$_{cat.}$$^{-1}$	-	-
		NO$_2^-$ + CO$_2$	0.1 M KHCO$_3$ + 0.1 M KNO$_2$	610.6 μg h^{-1} mg$_{cat.}$$^{-1}$	-	-
47	Zn/Cu	NO$_3^-$ + CO$_2$	0.1 M KHCO$_3$ + 500 ppm-N KNO$_3$	16 μmol h^{-1} cm^{-2}	75	CH$_3$NH$_2$, CH$_3$COOH, C$_2$H$_4$, HCOOH, H$_2$
48	CuO$_{50}$ZnO$_5$	NO$_3^-$ + CO$_2$	0.1 M Na$_2$SO$_4$ + 0.1 M NaNO$_3$	-	41	-
This work	Co-O-C	NO$_3^-$ + CO$_2$	0.1 M KHCO$_3$ + 0.05 M KNO$_3$	2704.2 ± 183.9 μg h^{-1} mg$_{cat.}$$^{-1}$ (H cell) 4648.2 ± 401.2 μg h^{-1} mg$_{cat.}$$^{-1}$ (flow cell)	31.4 ± 2.1 53.2 ± 4.6	CO, H$_2$, NO$_2^-$, NH$_3$
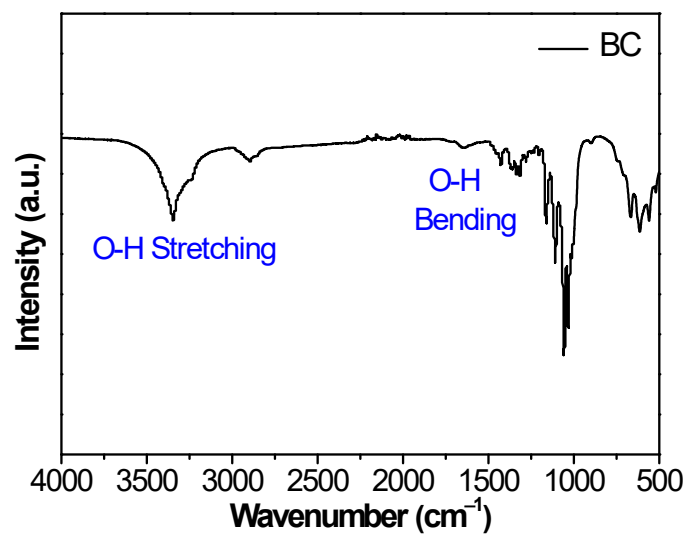
Fig. S1. FT-IR spectrum of pre-treated BC.
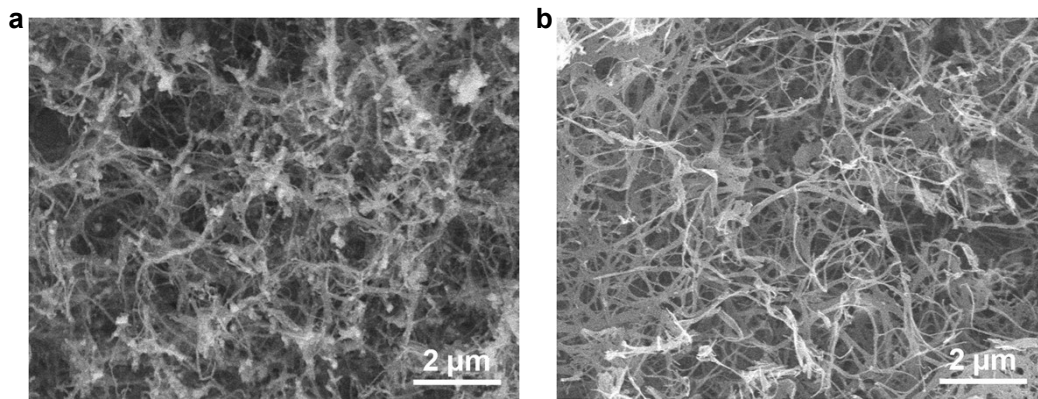
Fig. S2. SEM images of (**a**) Co-NPs/CBC and (**b**) Co-O-C samples.
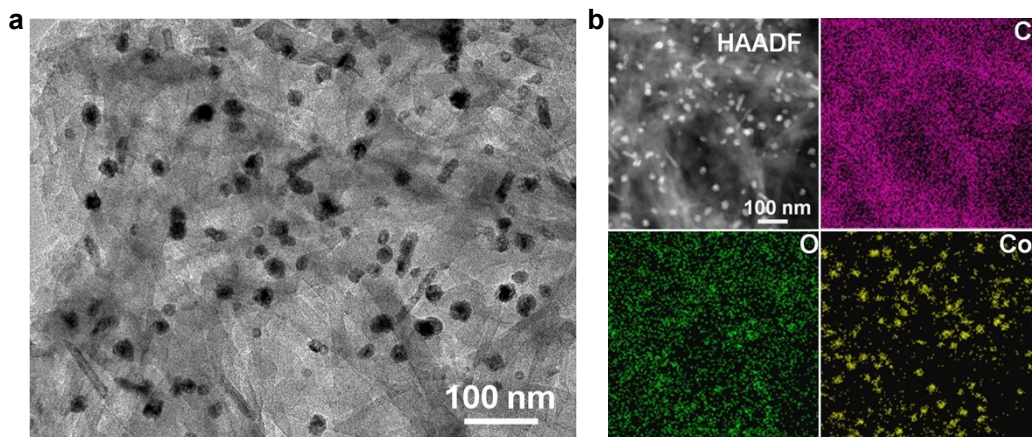
Fig. S3. (**a**) TEM image of Co-NPs/CBC sample. (**b**) Corresponding elemental mapping images of Co-NPs/CBC.

The transmission electron microscopy (TEM) image of Co-NPs/CBC displays homogeneous Co nanoparticles loaded onto carbon support (Fig. S3a). The corresponding elemental mapping analysis revealed that C, O and Co elements are homogeneously distributed over the entire sample (Fig. S3b)
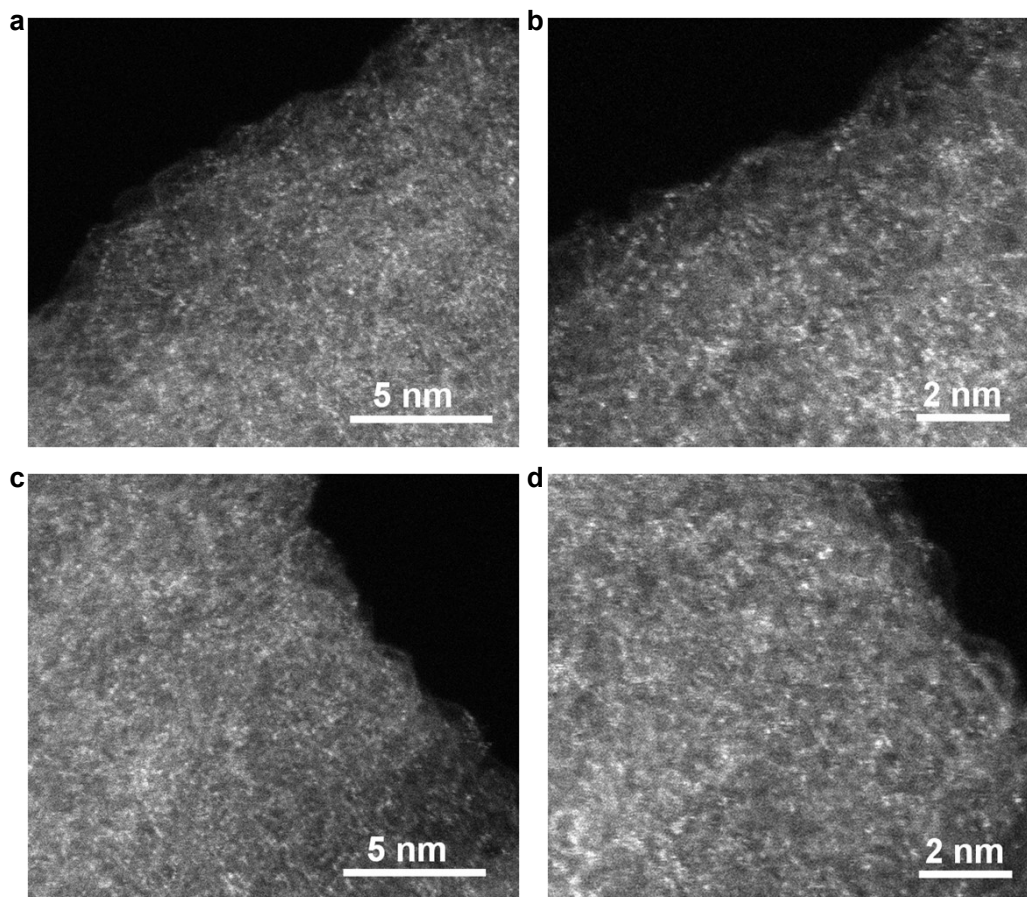
Fig. S4. Aberration-corrected HAADF-STEM images obtained from different locations of Co-O-C.
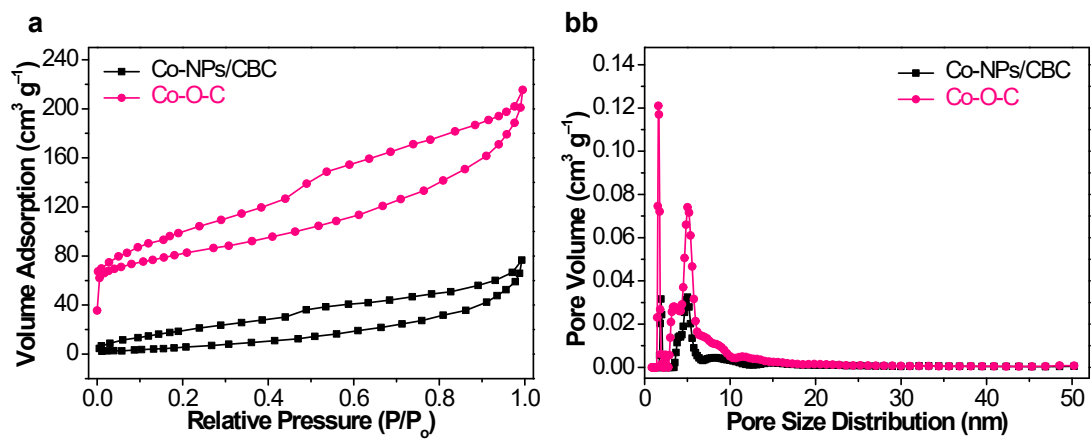
Fig. S5. (**a**) N_2 adsorption-desorption isotherms of Co-NPs/CBC and Co-O-C samples. (**b**) Corresponding pore size distribution curves.
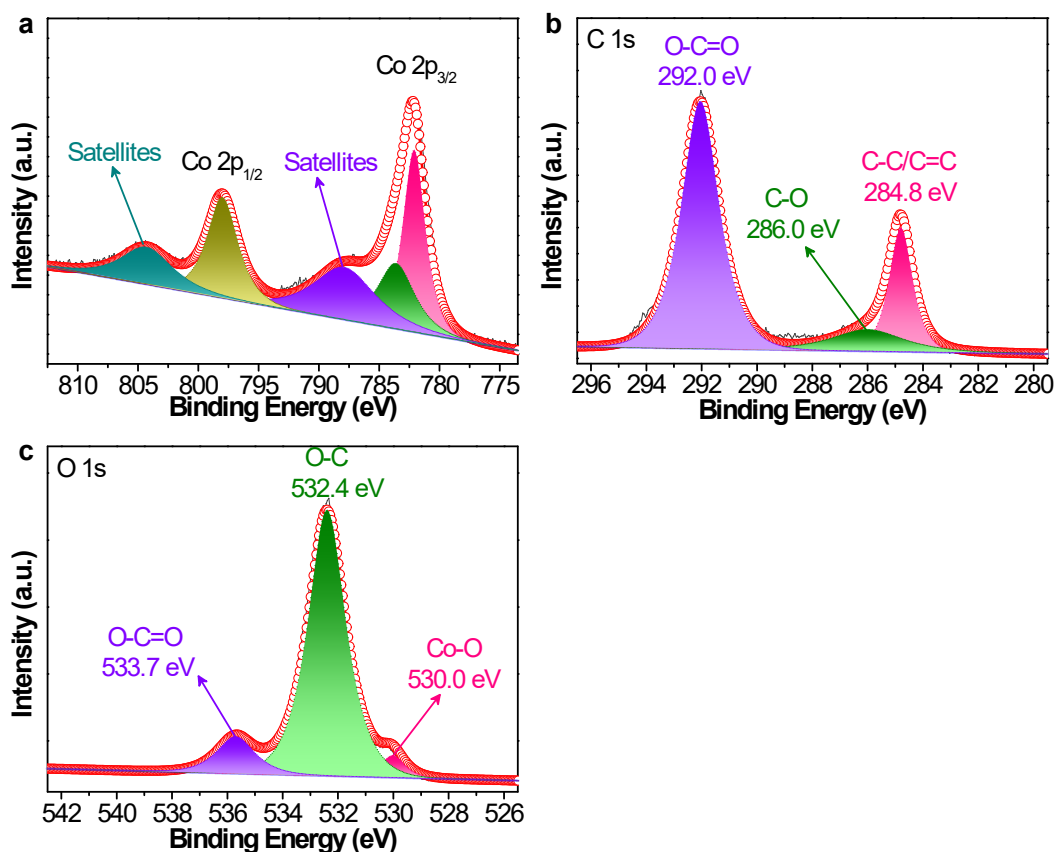
Fig. S6. High-resolution XPS spectra of (**a**) Co 2*p*, (**b**) C 1*s* and (**c**) O 1*s* of Co-NPs/CBC.

The Co 2p$_{3/2}$ core level region of Co-NPs/CBC (Fig. S6a) presents three peaks located at 782.1, 783.7 and 788.0 eV, corresponding to the oxidized cobalt species and specific shakeup satellite peak, respectively. The high-resolution C 1s and O 1s XPS spectra (Fig. S6b, c) indicate the existence of rich oxygen functional groups and the formation of weak Co-O bonds in Co-NPs/CBC.
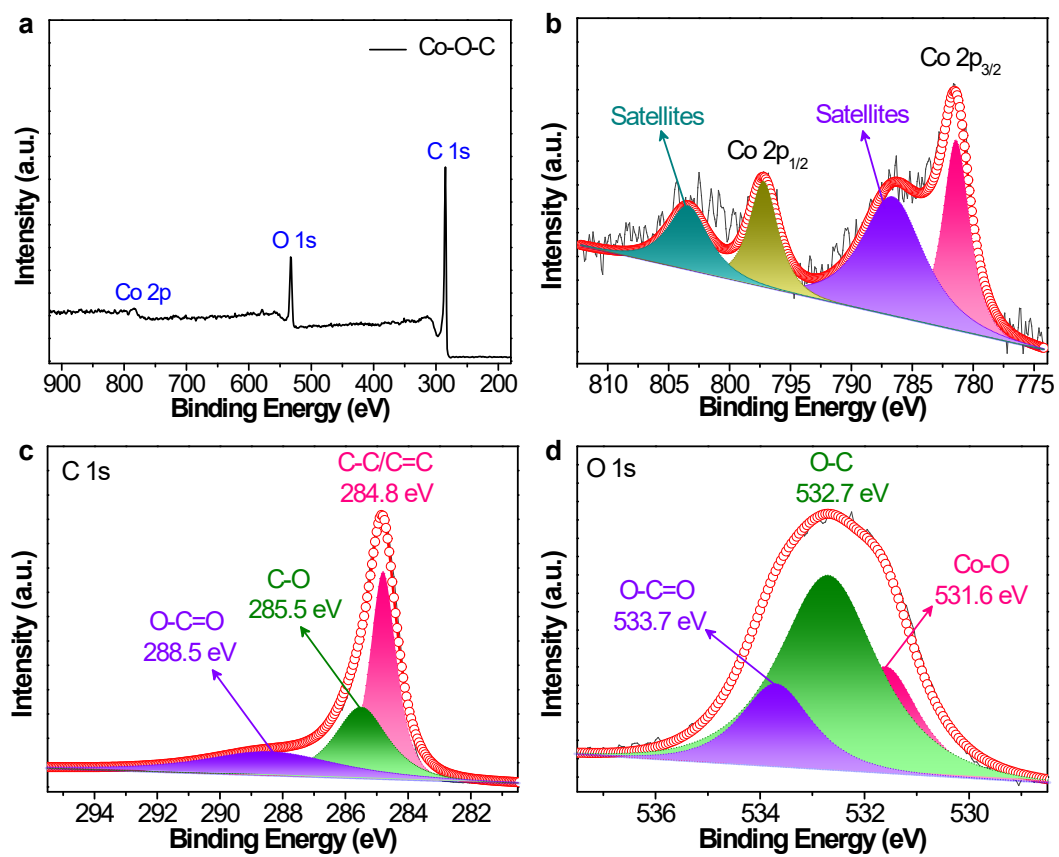
Fig. S7. (**a**) Survey XPS spectrum and high-resolution XPS spectra of (**b**) Co 2p, (**c**) C 1s and (**d**) O 1s of Co-O-C.
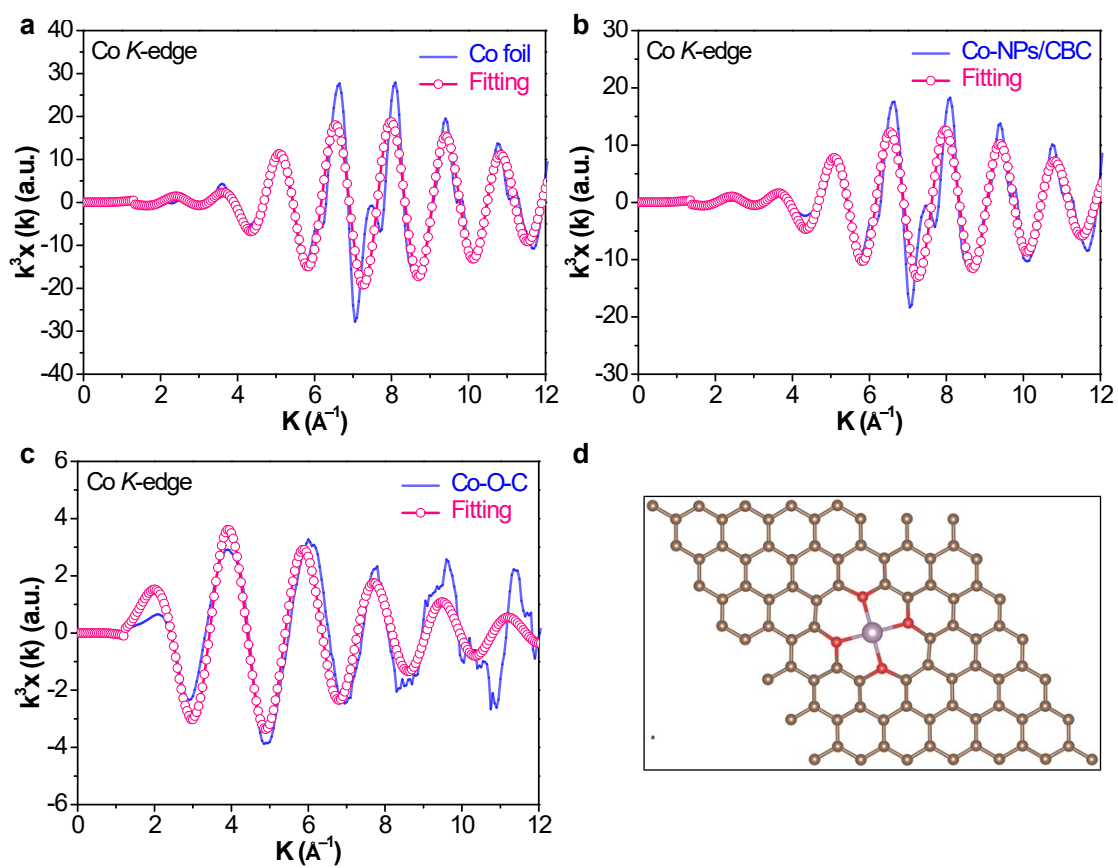
Fig. S8. Co *K*-edge EXAFS fitting curves of (**a**) Co foil, (**b**) Co-NPs/CBC and (**c**) Co-O-C at *k* space. (**d**) The proposed Co-$(O-C_2)_4$ structure (Gray: C, red: O, Purple: Co).
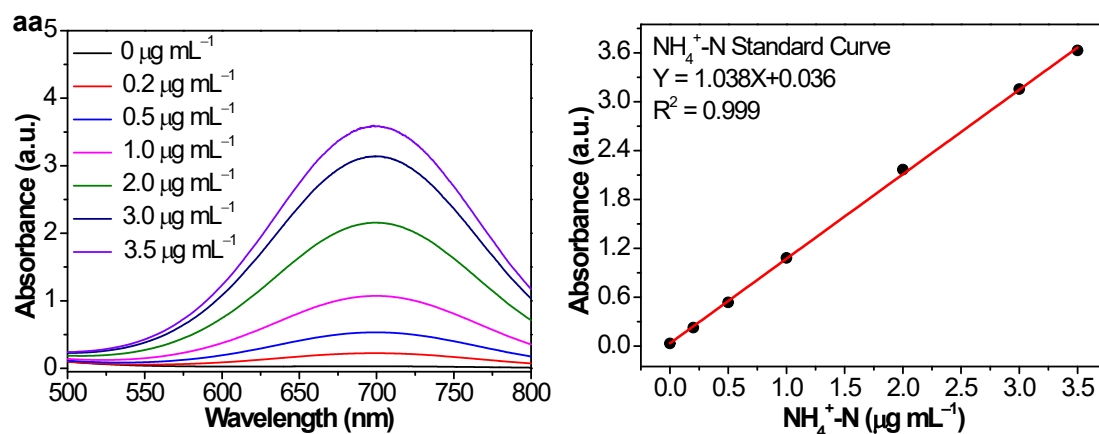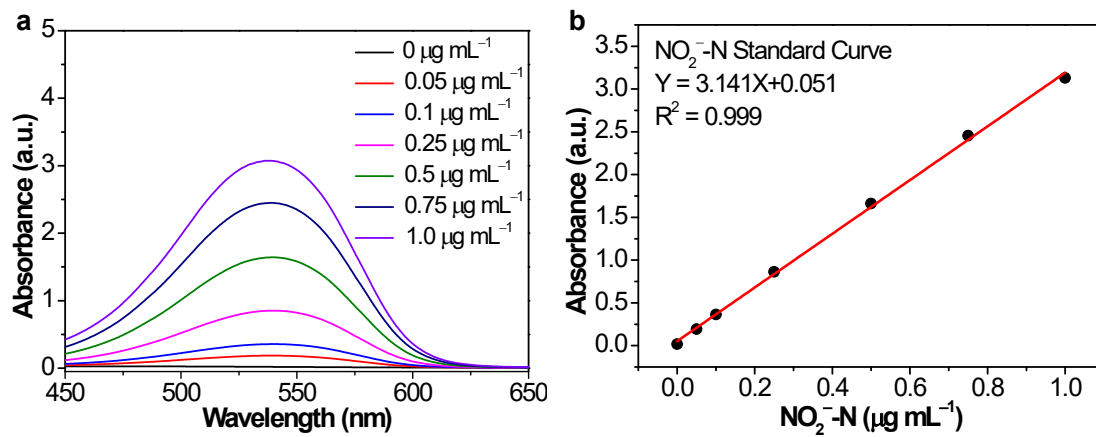
Fig. S9. (a) UV-Vis absorption spectra obtained from the solutions with different NH_4^+-N concentrations (0, 0.05, 0.10, 0.25, 0.50, 1.0, 2.0 and 3.0 μg mL^{-1}). **(b)** Calibration curve used to determine NH_4^+-N concentration.

For urease decomposition method, 0.4 mL of urease solution (5.0 mg mL^{-1}) was added into 3.6 mL of urea electrolyte, and then reacted at 37 °C in constant temperature shaker for 40 min. Urea was decomposed by urease into CO_2 and two NH_3 molecules. After the decomposition, NH_3 concentration of urea electrolyte with urease was detected *via* above indophenol blue method.
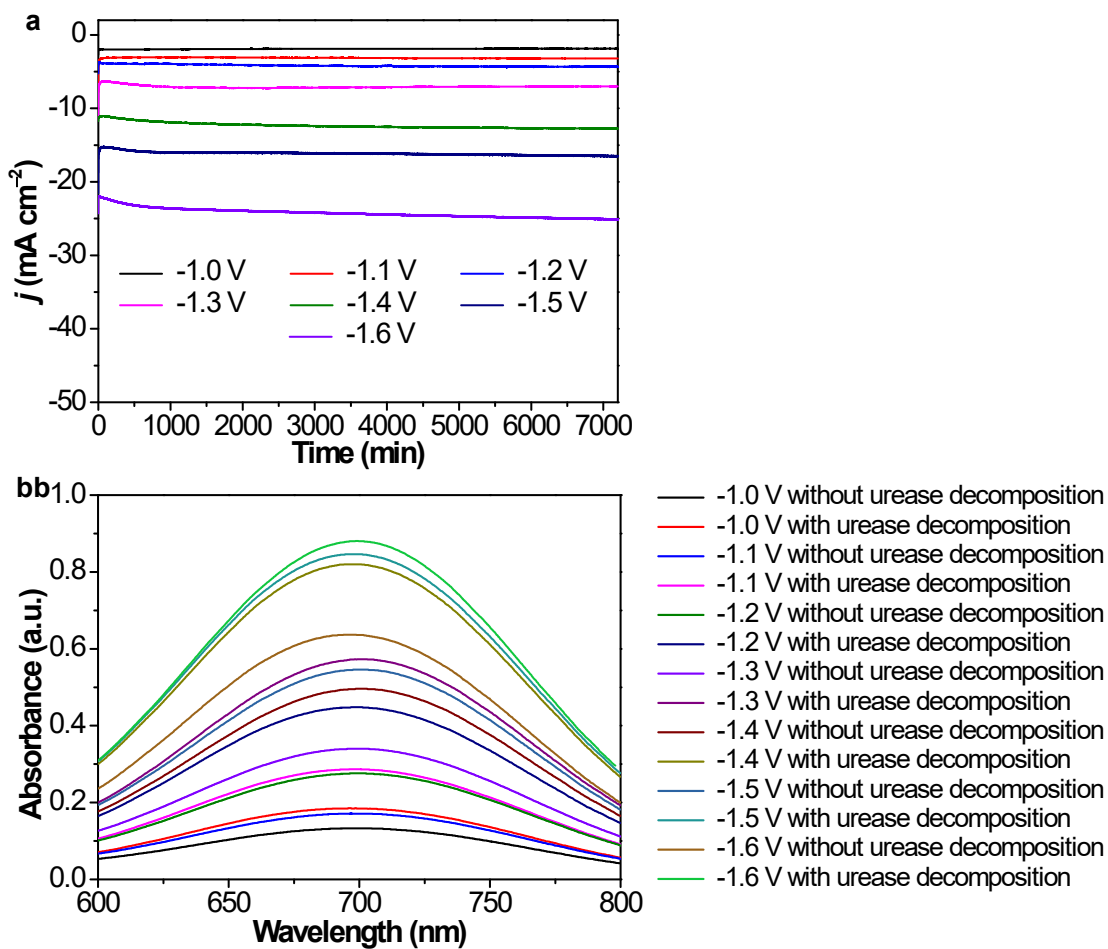
Fig. S10. (a) Time-dependent current density curves of Co-NPs/CBC at different applied potentials in CO$_2$-saturated 0.1 M KHCO$_3$ + 0.05 M KNO$_3$ electrolyte over a 2 h reaction period. **(b)** UV-Vis absorption spectra of the corresponding samples recorded in accordance with the indophenol blue method.
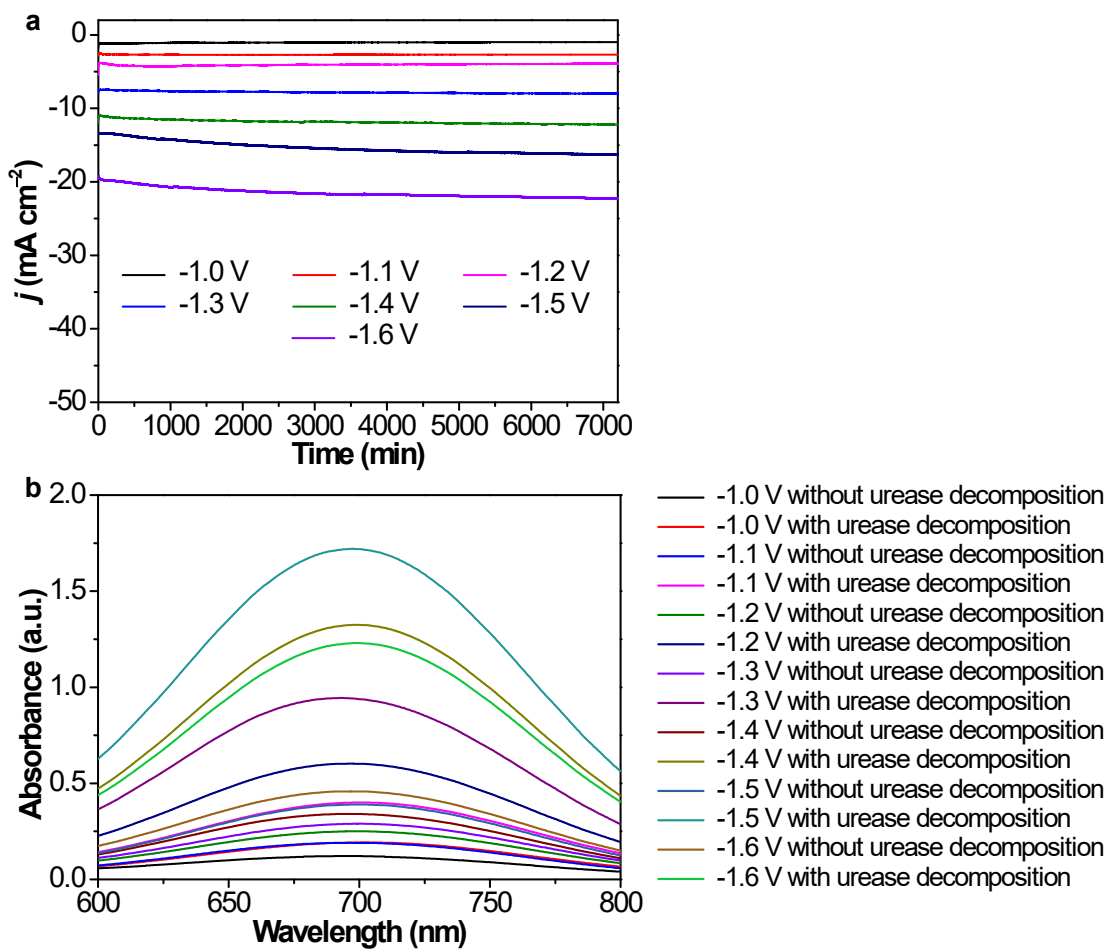
Fig. S11. (a) Time-dependent current density curves of Co-O-C at different applied potentials in CO$_2$-saturated 0.1 M KHCO$_3$ + 0.05 M KNO$_3$ electrolyte over a 2 h reaction period. **(b)** UV-Vis absorption spectra of the corresponding samples recorded in accordance with the indophenol blue method.
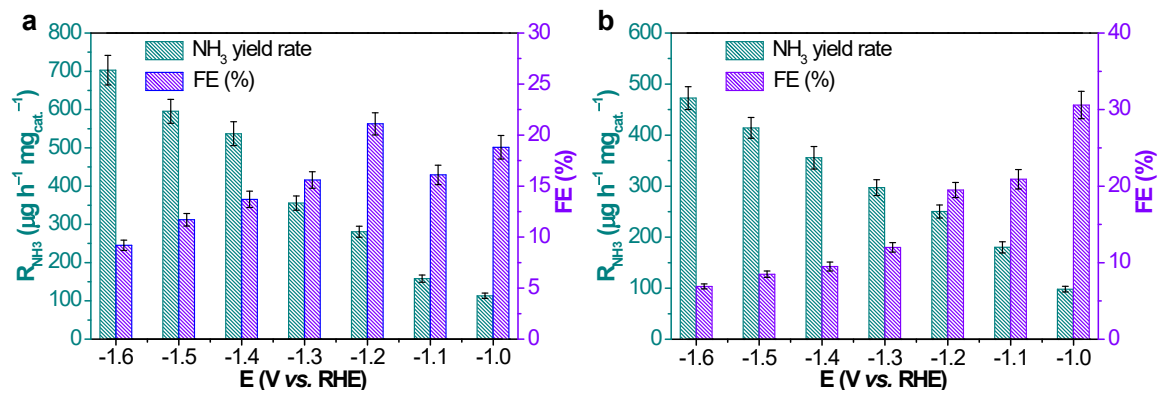
Fig. S12. R_{NH_3} and corresponding FE on (**a**) Co-NPs/CBC and (**b**) Co-O-C at different applied potentials.

Fig. S13. (**a**) UV-Vis absorption spectra obtained from the solutions with different NO_2^--N concentrations (0, 0.05, 0.1, 0.25, 0.5, 0.75 and 1.0 μg mL^{-1}). (**b**) Calibration curve used to determine NO_2^--N concentration.
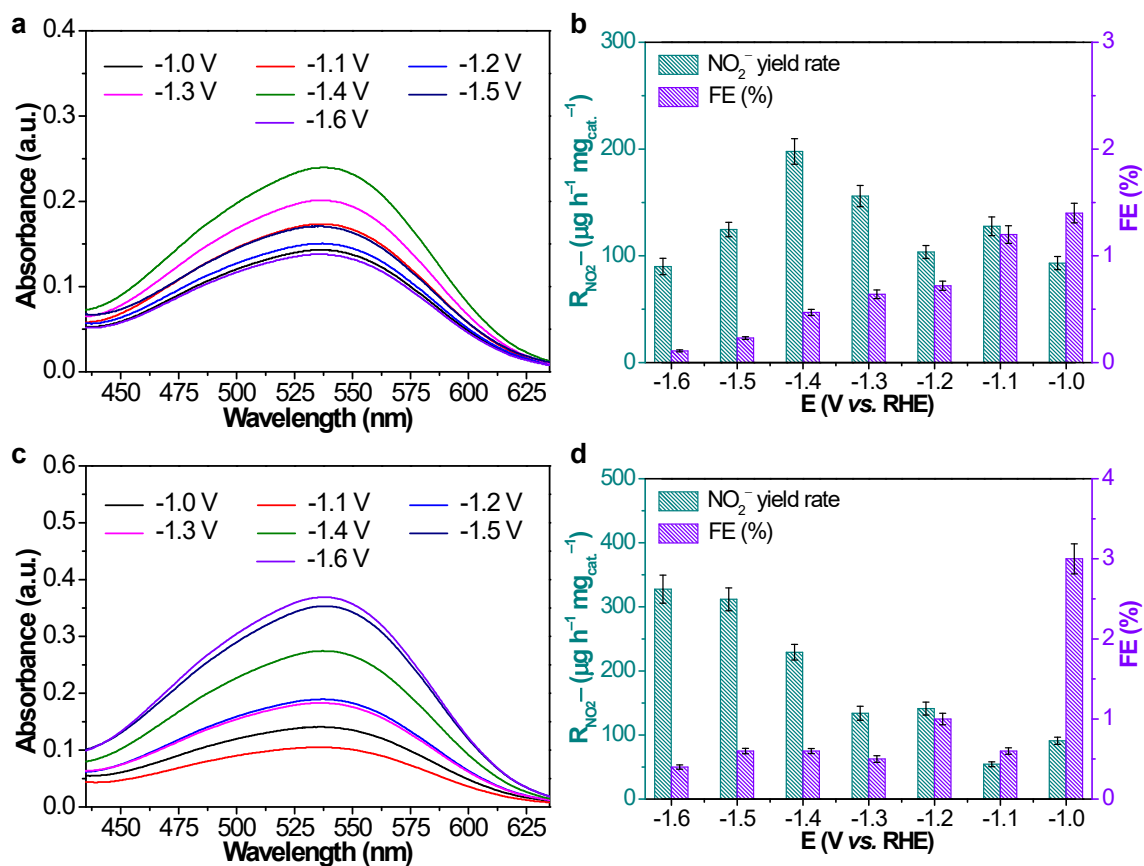
Fig. S14. (**a**) UV-Vis absorption spectra of Co-NPs/CBC at different applied potentials. (**b**) Dependence of $R_{NO_2^-}$ and FE on the applied potentials. (**c**) UV-Vis absorption spectra of Co-O-C at different applied potentials. (**d**) Dependence of $R_{NO_2^-}$ and FE on the applied potentials.
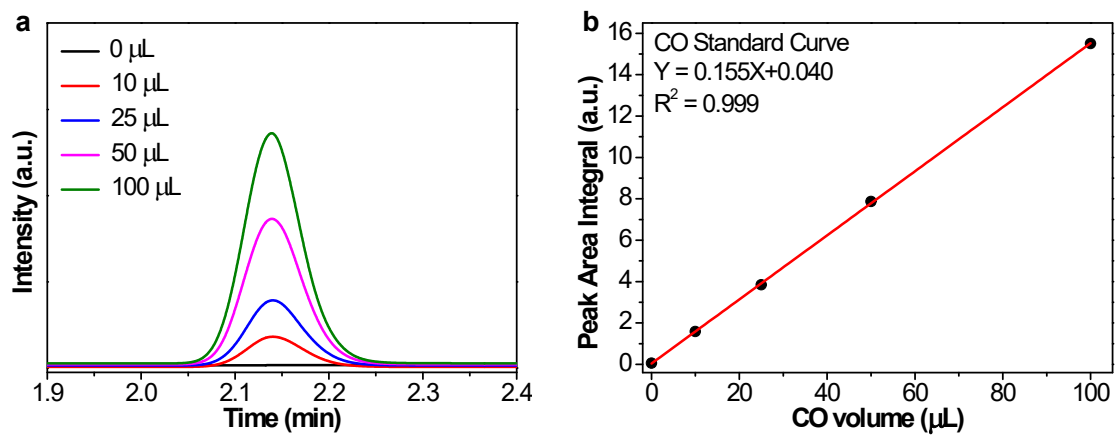
Fig. S15. Determination of CO by the gas chromatography (GC). (**a**) Chromatograms of the CO standards and (**b**) Corresponding calibration curve.
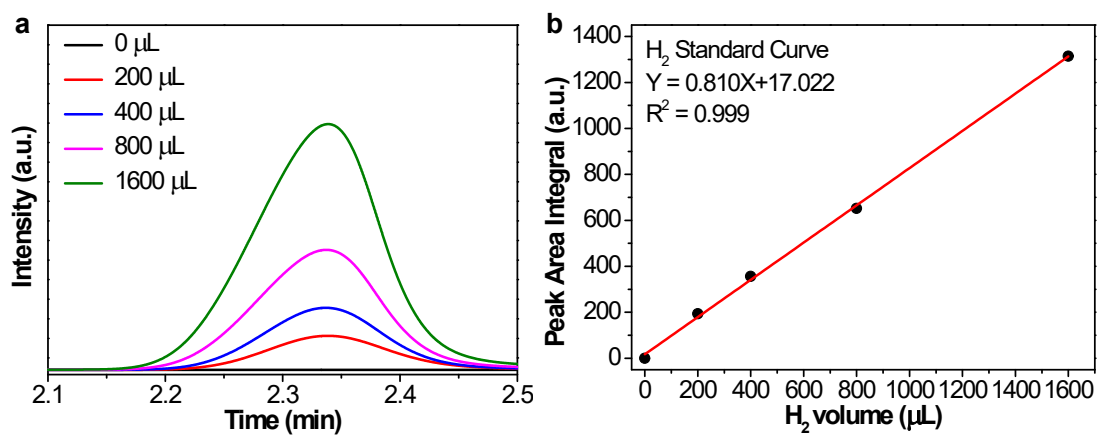
Fig. S16. Determination of H_2 by the gas chromatography (GC). (**a**) Chromatograms of the H_2 standards and (**b**) Corresponding calibration curve.
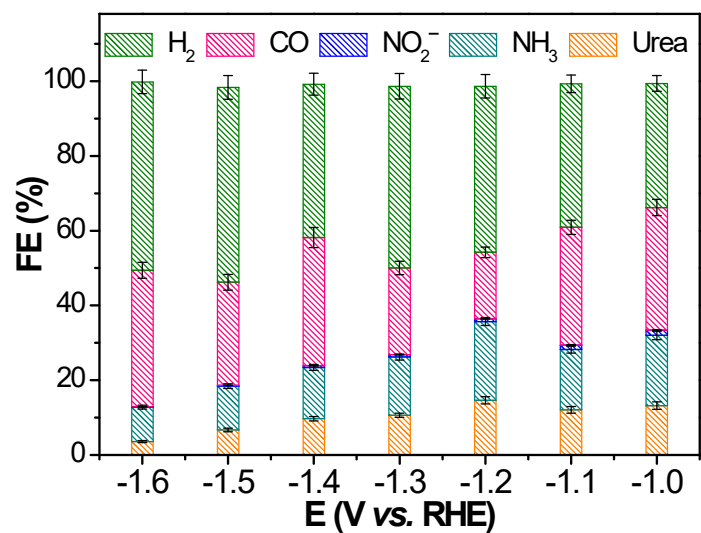
Fig. S17. FE distribution of all electrocatalytic products obtained from Co-NPs/CBC catalyzed urea synthesis at different applied potentials.
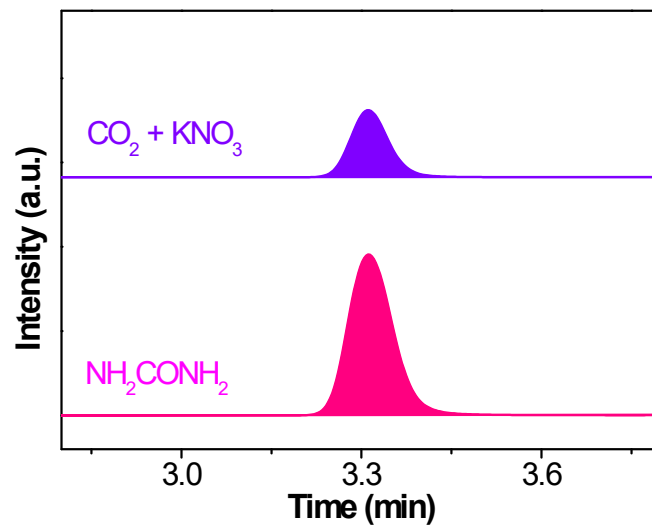
Fig. S18. The high-performance liquid chromatography (HPLC) spectra of produced urea over Co-O-C and standard urea solution.
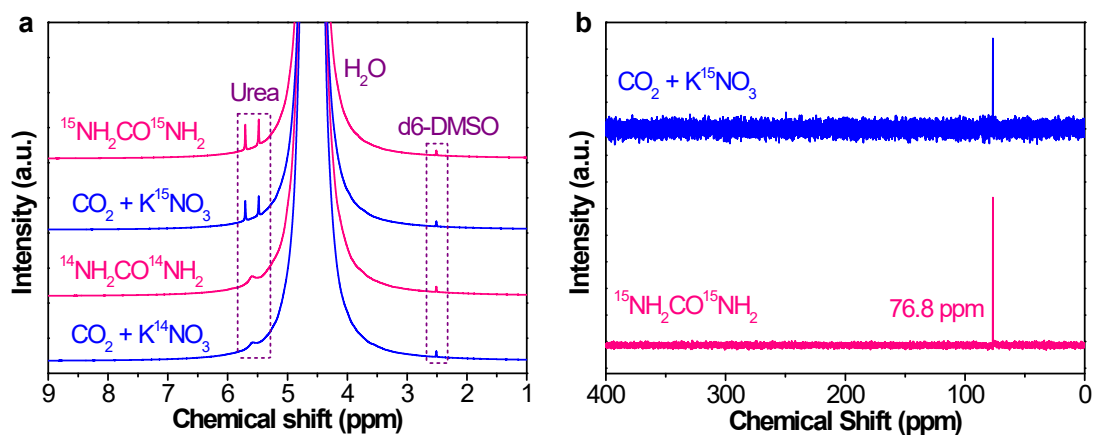
Fig. S19. (a) ^1H NMR spectra of 0.1 M $KHCO_3$ + 0.05 M $K^{14}NO_3/K^{15}NO_3$ electrolytes saturated with CO_2 after 2 h of electrolysis over Co-O-C and standard $^{14}NH_2CO^{14}NH_2/^{15}NH_2CO^{15}NH_2$ solutions. (b) ^{15}N NMR spectra of 0.1 M $KHCO_3$ + 0.05 M $K^{15}NO_3$ electrolytes saturated with CO_2 after 2 h of electrolysis and standard $^{15}NH_2CO^{15}NH_2$ solutions.
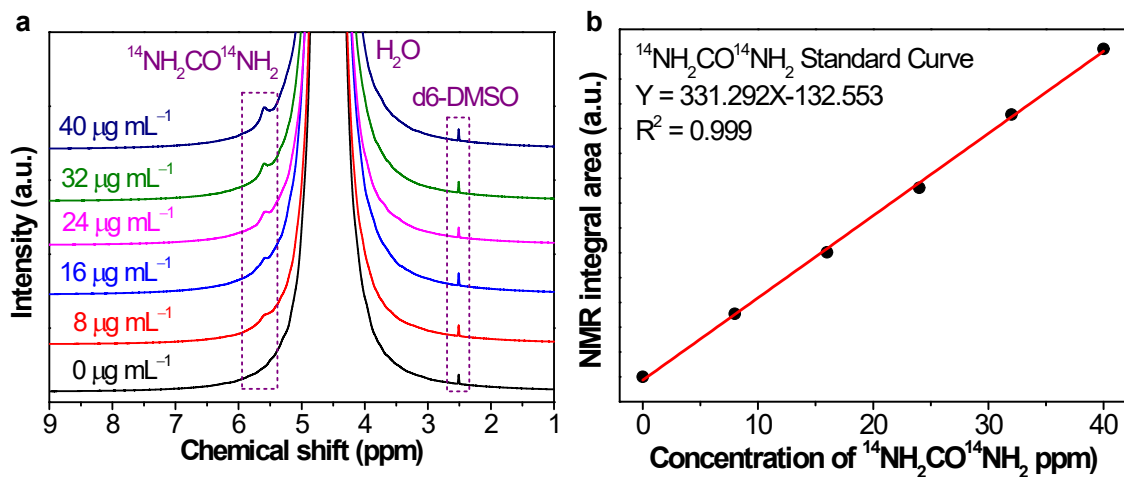
Fig. S20. (**a**) ^1H NMR spectra of $^{14}NH_2CO^{14}NH_2$ standards. (**b**) The corresponding $^{14}NH_2CO^{14}NH_2$ calibration curve.

Urea standards were prepared by dissolving different qualities of urea in mixed solutions of 0.1 M $KHCO_3$ + 0.05 M KNO_3. The concentration of urea exhibits a linear relationship with the integral area of characteristic peak, thus the concentration of the products could be calculated *via* the fitting formula of the calibration curves.
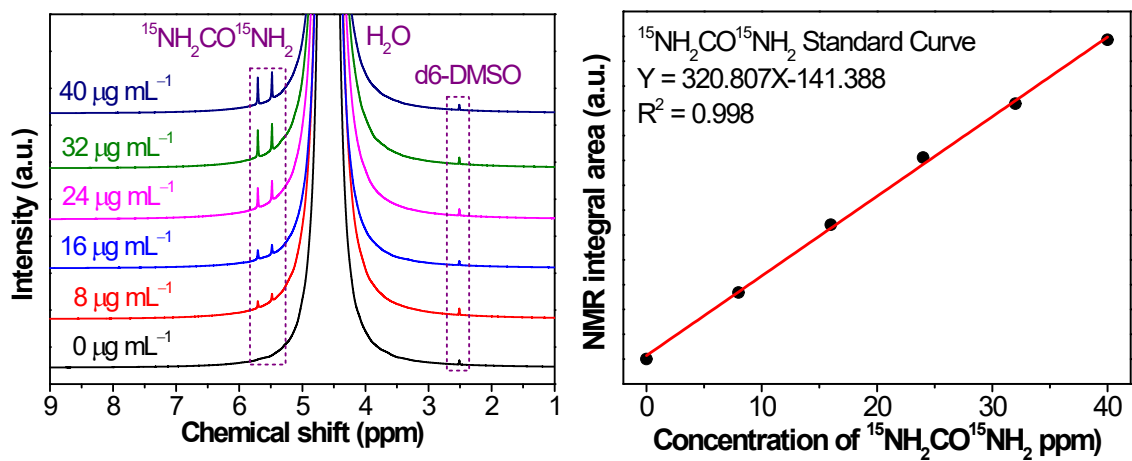
Fig. S21. (**a**) ^{1}H NMR spectra of ^{15}NH$_2$CO^{15}NH$_2$ standards. (**b**) The corresponding ^{15}NH$_2$CO^{15}NH$_2$ calibration curve.
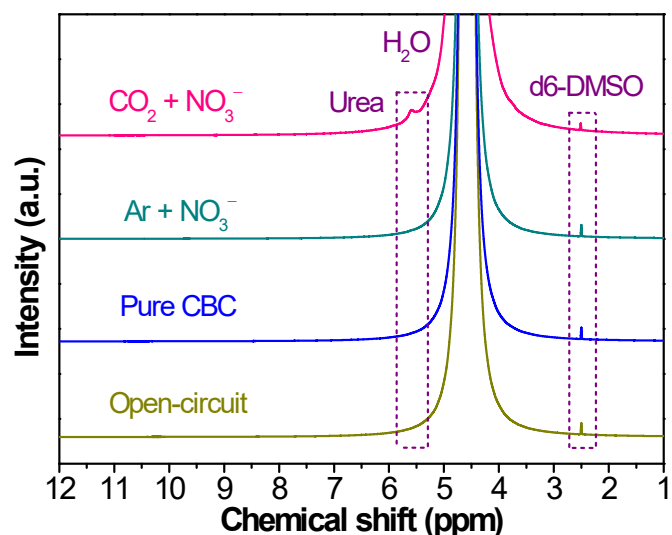
Fig. S22. ^{1}H NMR spectra of the samples obtained at different conditions.

^{1}H NMR spectra of Co-O-C in the CO_2-saturated 0.1 M $KHCO_3$ + 0.05 M KNO_3, Co-O-C in Ar-saturated 0.1 M $KHCO_3$ + 0.05 M KNO_3 solution and pure CBC in CO_2-saturated 0.1 M $KHCO_3$ + 0.05 M KNO_3 solution at −1.5 V (*vs.* RHE), as well as Co-O-C in CO_2-saturated 0.1 M $KHCO_3$ + 0.05 M KNO_3 solution under open-circuit potential (OCP).
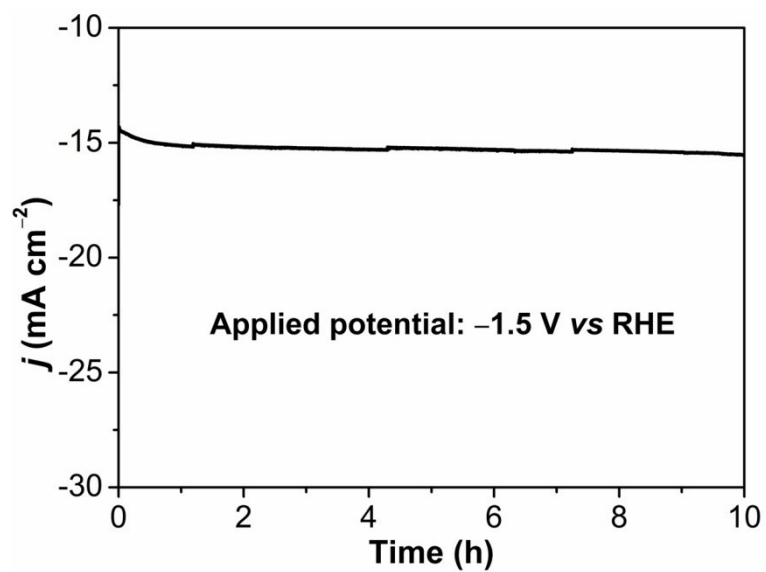
Fig. S23. Time-dependent current density curves of Co-O-C at −1.5 V (*vs.* RHE) in CO$_2$-saturated 0.1 M KHCO$_3$ + 0.05 M KNO$_3$ for 10 h.
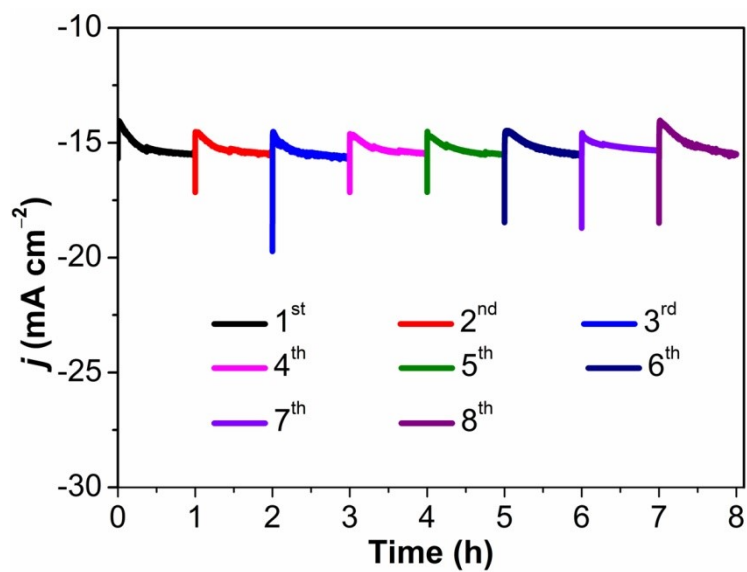
Fig. S24. Cycling stability test of Co-O-C at −1.5 V (*vs.* RHE) in CO_2-saturated 0.1 M $KHCO_3$ + 0.05 M KNO_3 for 8 cycles with 1 h reaction period per cycle.
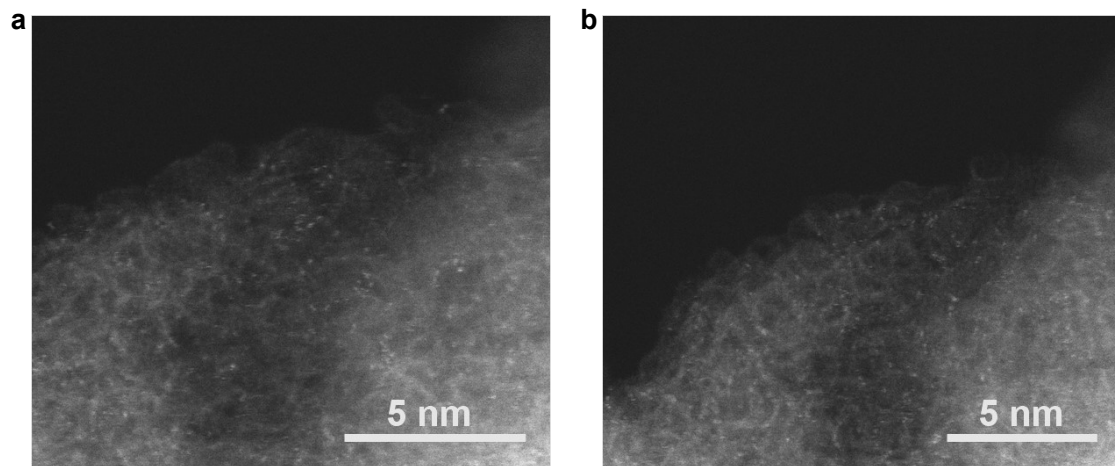
Fig. S25. High-magnification aberration-corrected HAADF-STEM images of Co-O-C after 8 consecutive cycles.
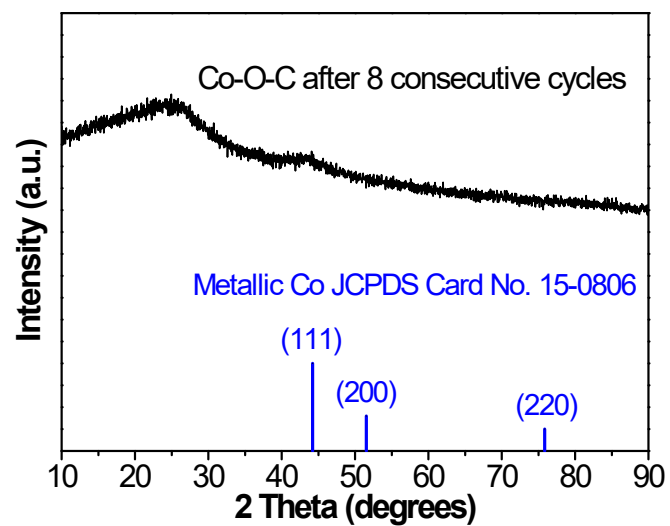
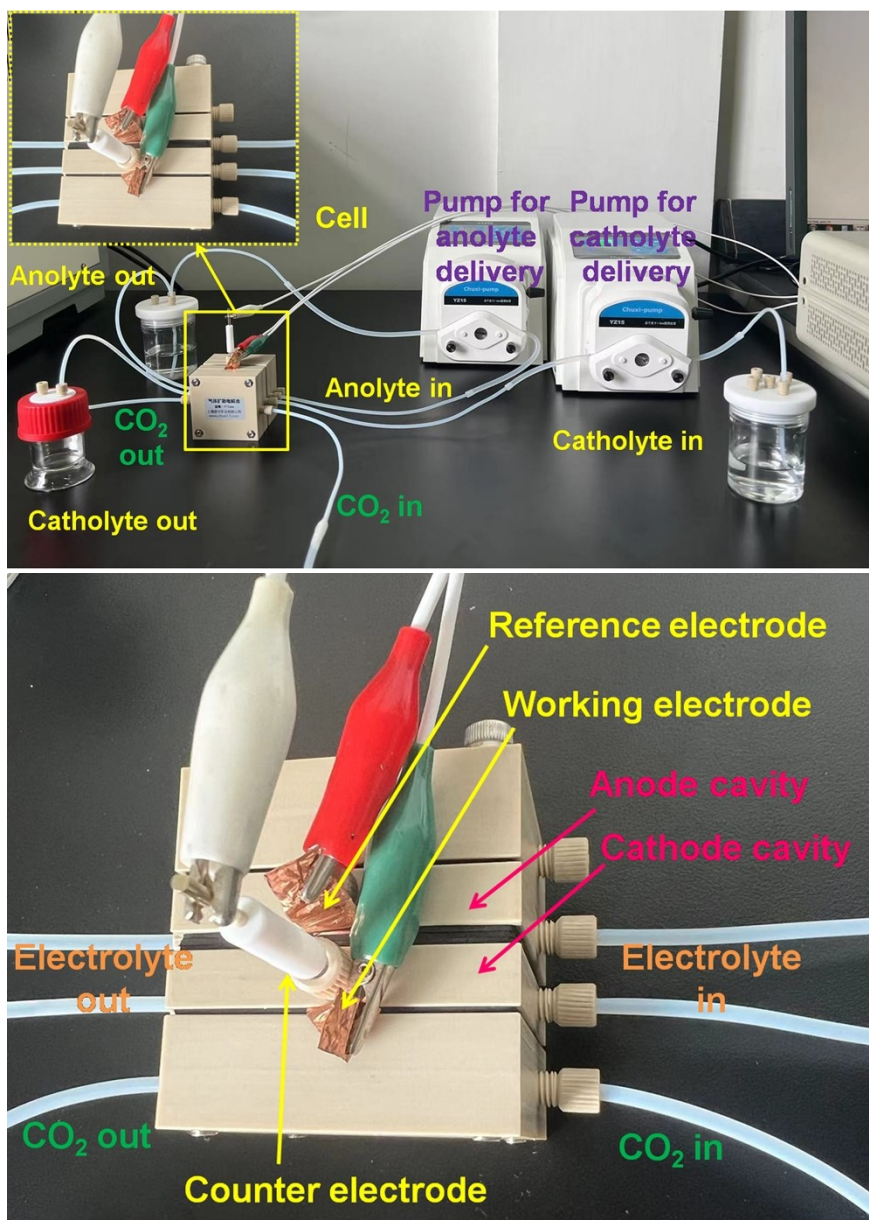**Fig. S26.** XRD pattern of Co-O-C after 8 consecutive cycles.

Fig. S27. The physical photographs of flow-cell reaction system and reactor for electrocatalytic urea synthesis.
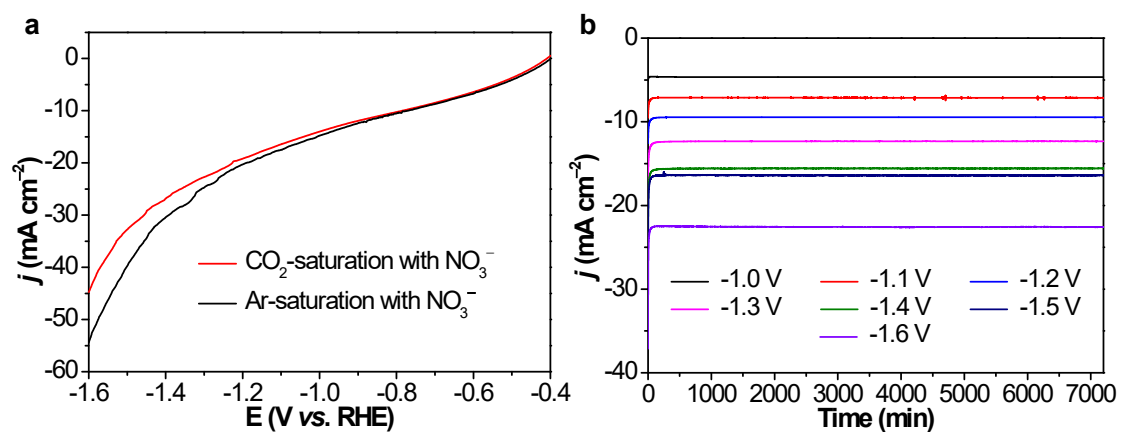
Fig. S28. (a) LSV curve of Co-O-C in 0.1 M KHCO$_3$ + 0.05 M KNO$_3$ electrolyte with Ar or CO$_2$ feeding gas in a flow cell. **(b)** Time-dependent current density curves of Co-O-C at different applied potentials in CO$_2$-saturated 0.1 M KHCO$_3$ + 0.05 M KNO$_3$ electrolyte over a 2 h reaction period in a flow cell.
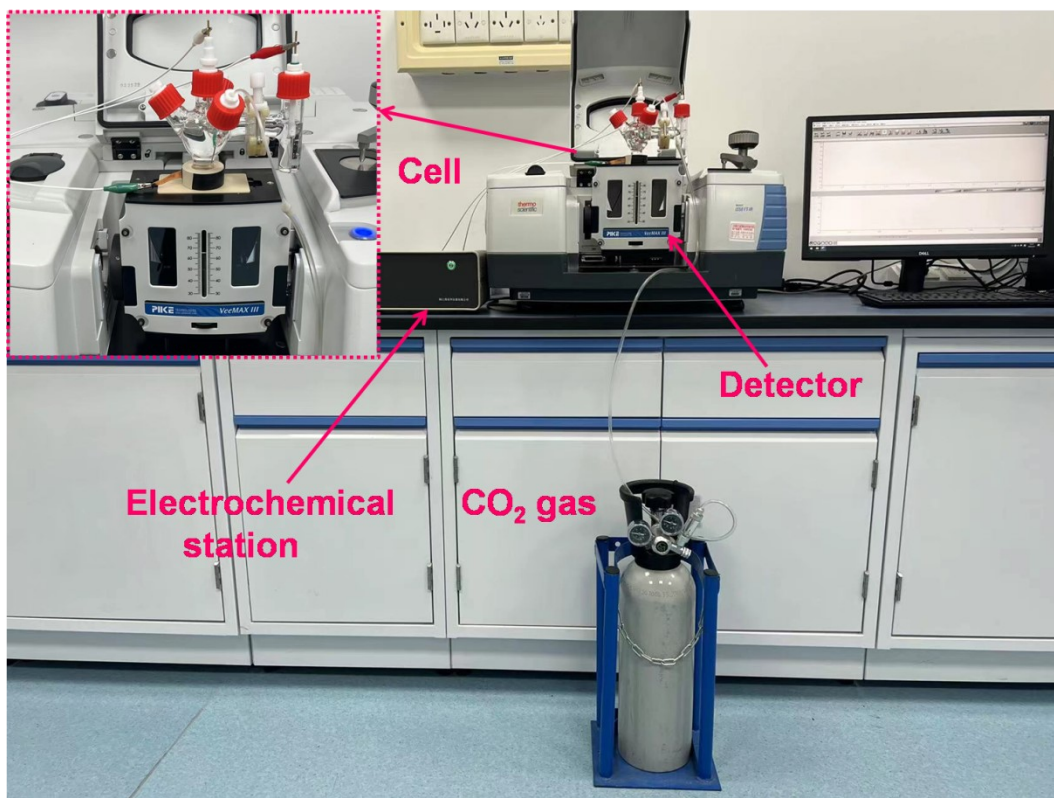
Fig. S29. The physical photographs of *operando* ATR-SEIRAS measurements system and reactor for electrocatalytic urea synthesis.
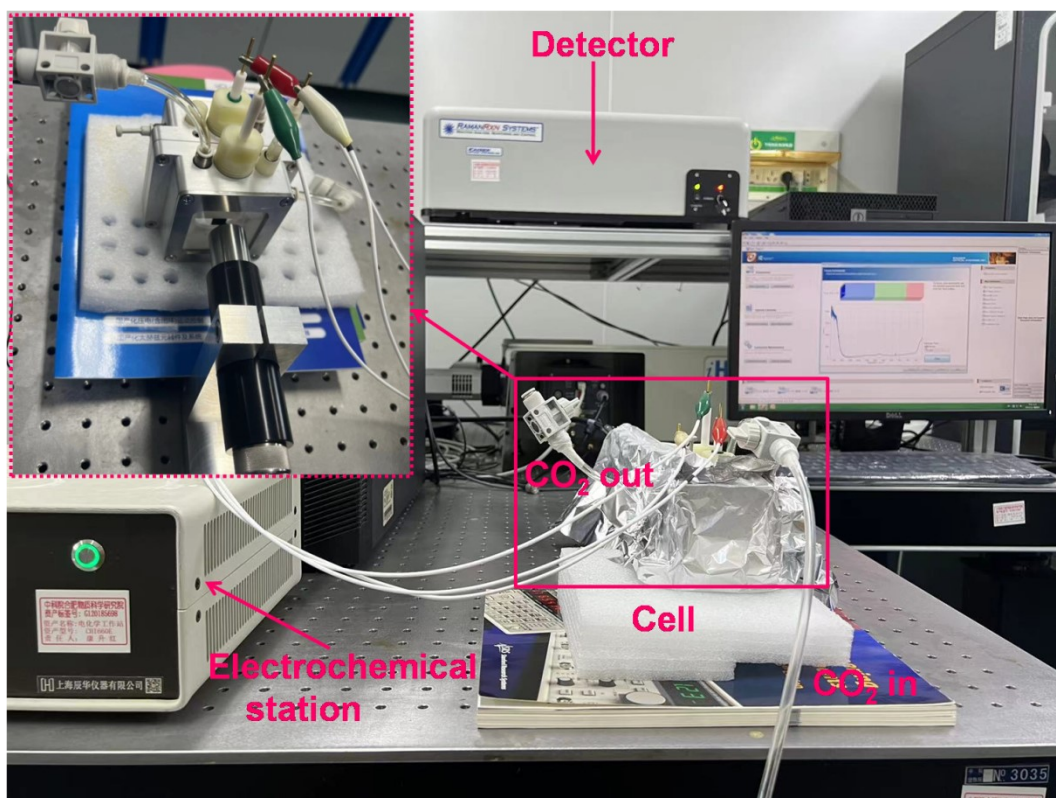
Fig. S30. The physical photographs of *operando* Raman measurements system and reactor for electrocatalytic urea synthesis.
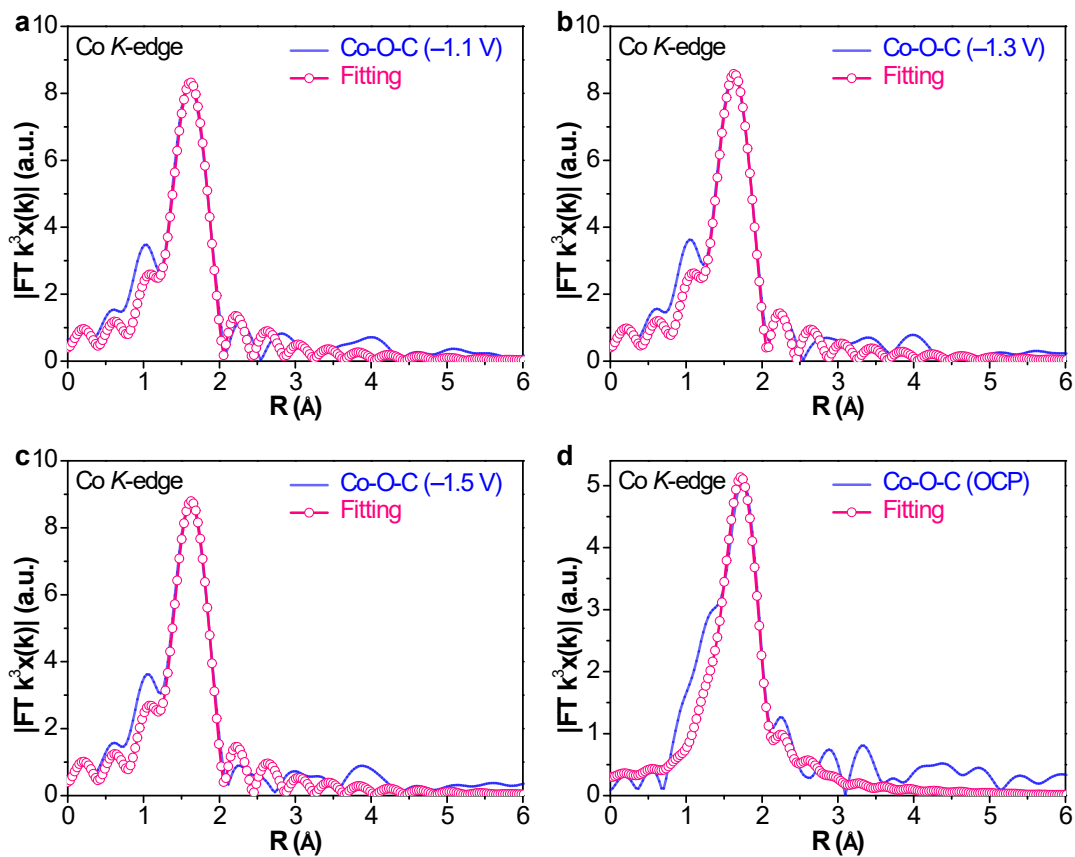
Fig. S31. Co *K*-edge EXAFS fitting curves of Co-O-C at *R* space under (**a**) −1.1 V (*vs.* RHE), (**b**) −1.3 V (*vs.* RHE), (**c**) −1.5 V (*vs.* RHE) and (**d**) OCP at *R* space.
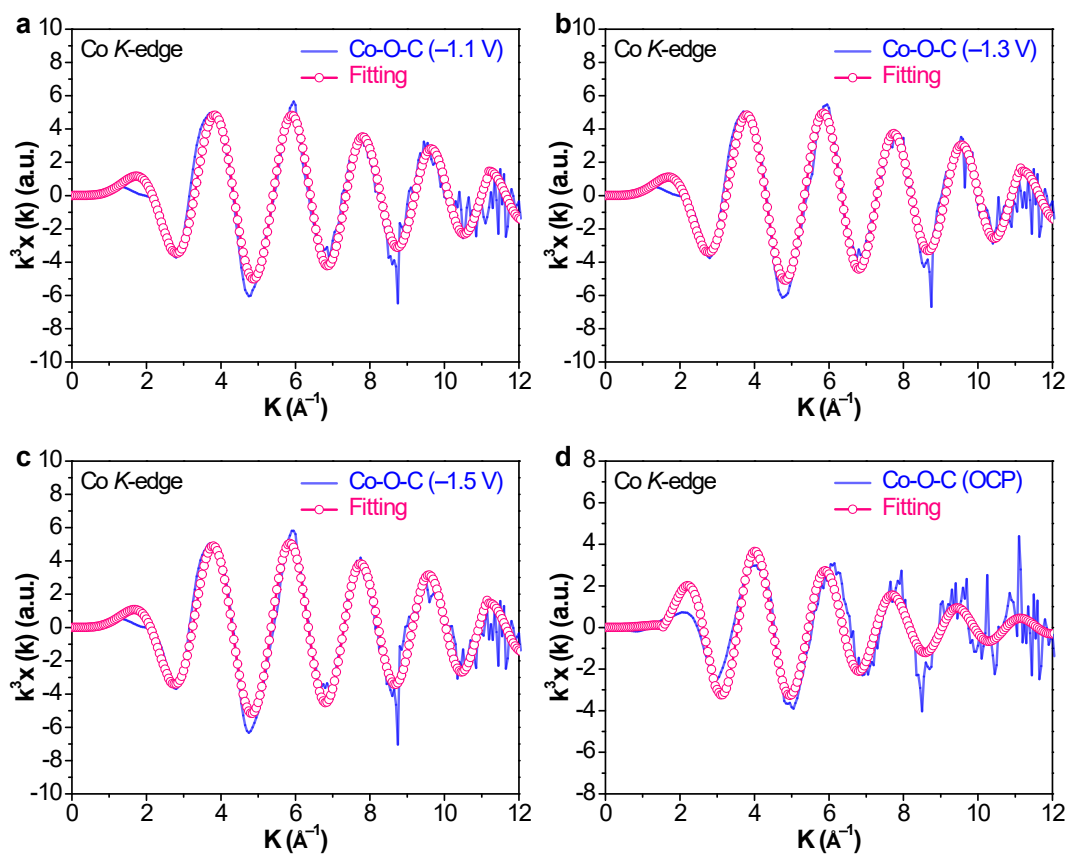
Fig. S32. Co K-edge EXAFS fitting curves of Co-O-C at R space under (**a**) −1.1 V (*vs.* RHE), (**b**) −1.3 V (*vs.* RHE), (**c**) −1.5 V (*vs.* RHE) and (**d**) OCP at k space.
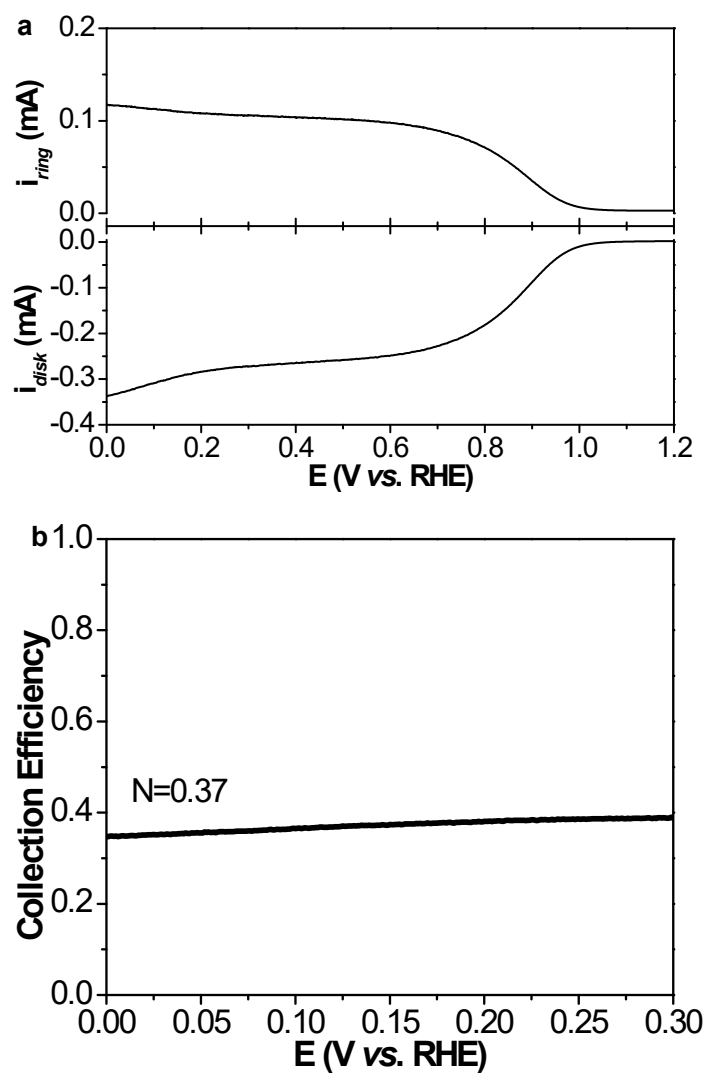
Fig. S33. (**a**) LSV curves of the bare RRDE in Ar-saturated 0.1 M $KHCO_3$ + 0.05 M KNO_3 electrolyte containing 2.0 mmol $K_3[Fe(CN)_6]$ at 1600 rpm to calibrate the collection efficiency. (**b**) Calculated collection efficiency (N) based on LSV result *via* dividing the ring current by the disk current.
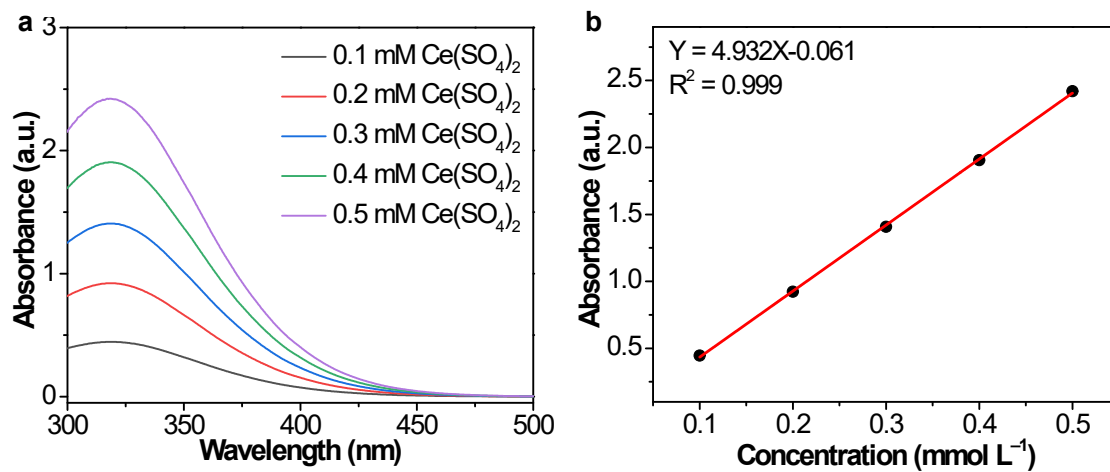
Fig. S34. (**a**) UV-vis spectra of Ce^{4+} solution with various concentrations. (**b**) The corresponding standard curve.
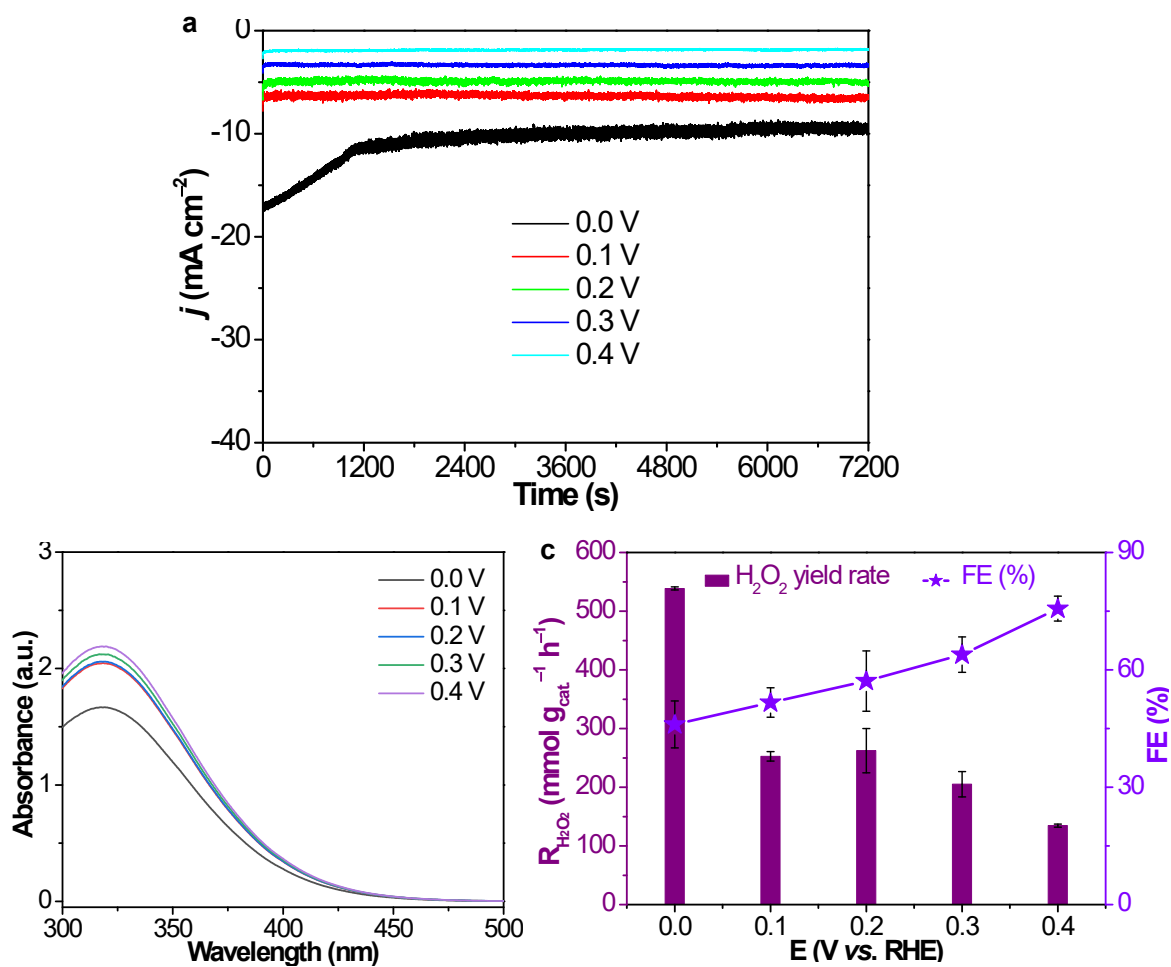
Fig. S35. (**a**) Time-dependent current density curves of Co-O-C at different applied potentials in O$_2$-saturated 0.1 M KHCO$_3$ + 0.05 M KNO$_3$ electrolyte over a 2 h reaction period. (**b**) UV-vis absorption spectra of Ce^{4+} solutions after injecting electrolytes at different potentials. (**c**) Dependence of H$_2$O$_2$ yield rate and FE on the applied potentials.
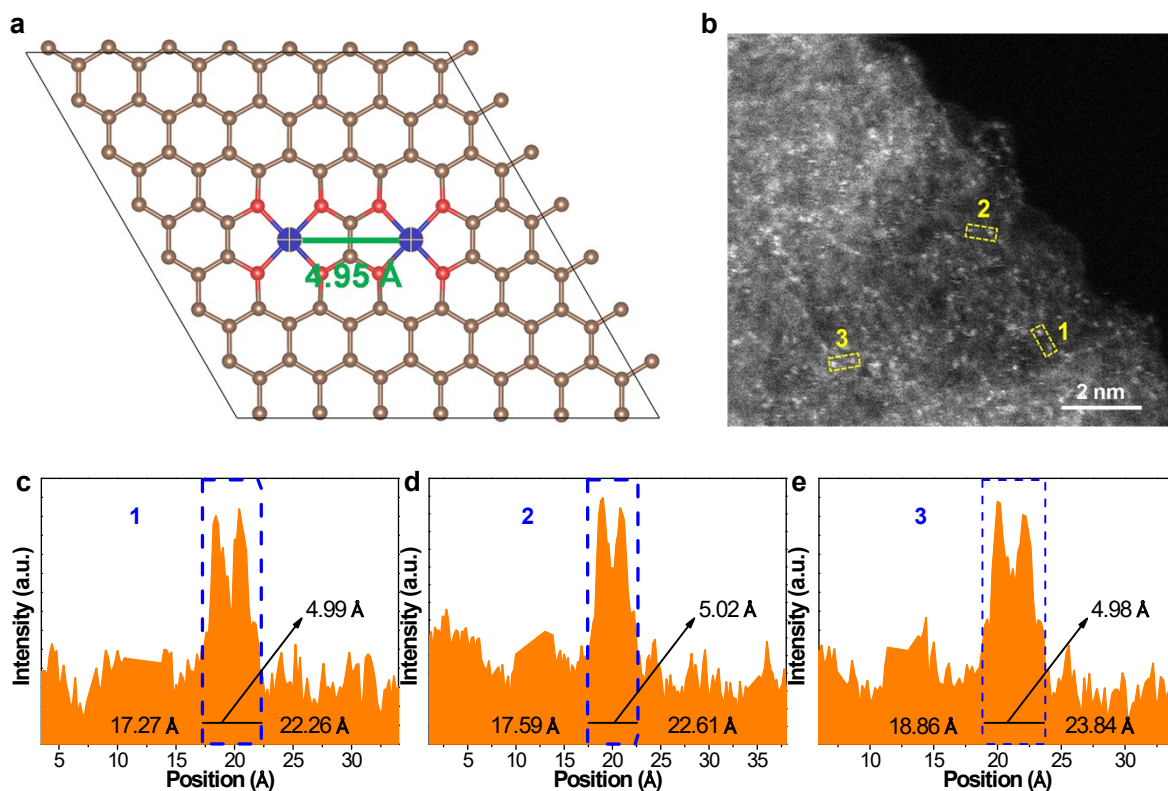
Fig. S36. (**a**) DFT optimised configuration of Co-(O-C$_2$)$_4$. Gray sphere: C, red sphere: O, Blue sphere: Co. (**b**) Aberration-corrected HAADF-STEM image of Co-O-C. (**c**)-(**e**) Corresponding intensity profiles obtained on the zoomed areas in panel (**b**).

Fig. S36a shows the optimized Co-(O-C$_2$)$_4$ configuration of eight Co-O bonds with the Co-Co bond length of 4.95 Å. We then conducted the aberration corrected high resolution TEM (HRTEM) with sub-Angstrom resolution to calculate the distance between the two adjacent Co atoms. HAADF-STEM results (Fig. S36b) revealed the homogeneously distributed small bright dual dots in a porous carbon matrix, attributed to heavy Co than light O and C atoms. The distance between two adjacent Co atoms tagged by red circles from different locations of Co-O-C is ~5.0 Å (Fig. S36c-e), which is essentially consistent with the theoretical value.

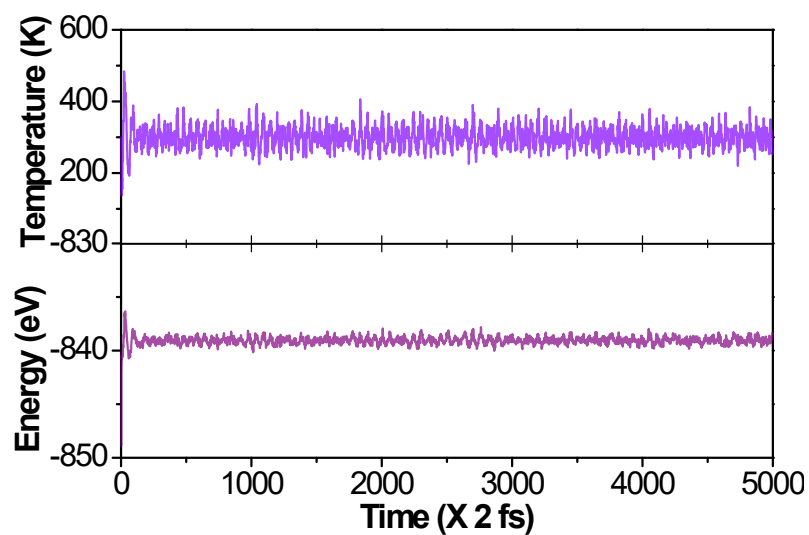**Fig. S37.** Variations of temperature and energy *vs* time for AIMD simulations of Co-(O-C$_2$)$_4$. The simulation is run under 300 K for 10 ps with a time step of 2 fs.
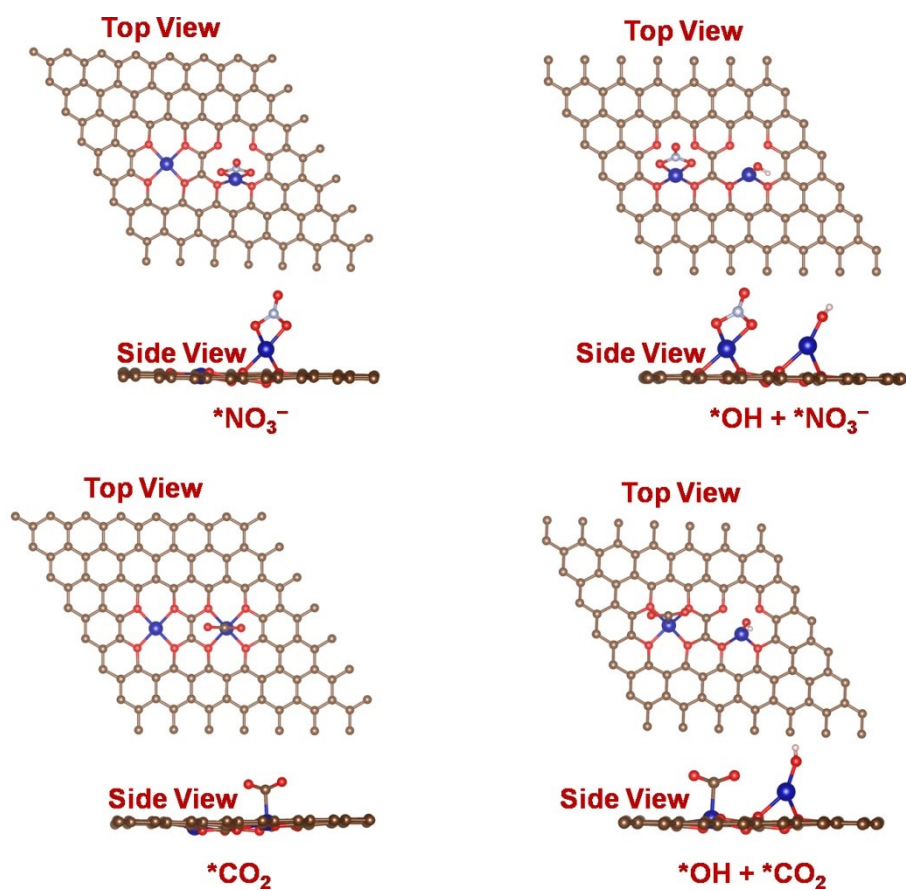
Fig. S38. DFT optimised configurations of $*NO_3^-$ and $*CO_2$ adsorption on the $Co-(O-C_2)_4$ and $*OH-Co-(O-C_2)_4$ sites. The blue, red, grey and white balls represent Co, O, C and H atoms, respectively.

Fig. S39. Top view of corresponding intermediates structures for each step. The blue, red, light blue, grey and white balls represent Co, O, N, C and H atoms, respectively.

Fig. S40. Side view of corresponding intermediates structures for each step. The blue, red, light blue, grey and white balls represent Co, O, N, C and H atoms, respectively.
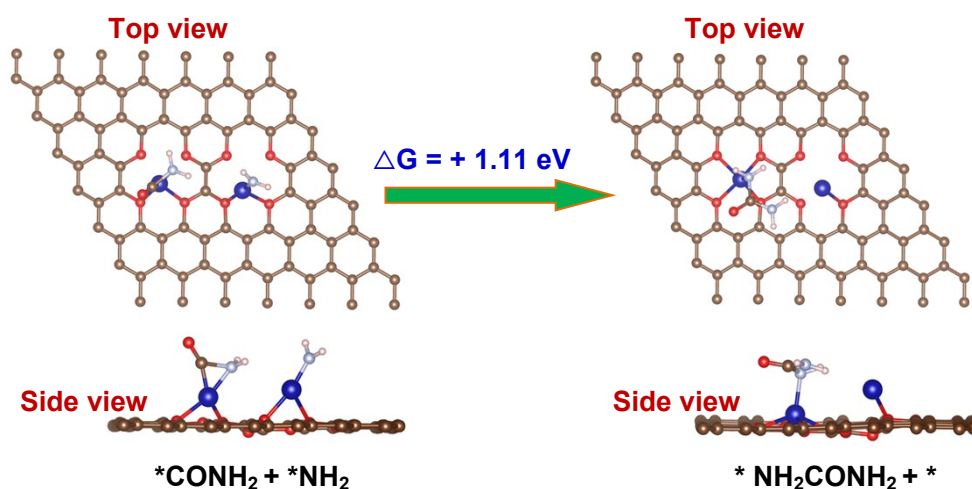
Fig. S41. Corresponding intermediates structures of intermediates in urea synthesis process.
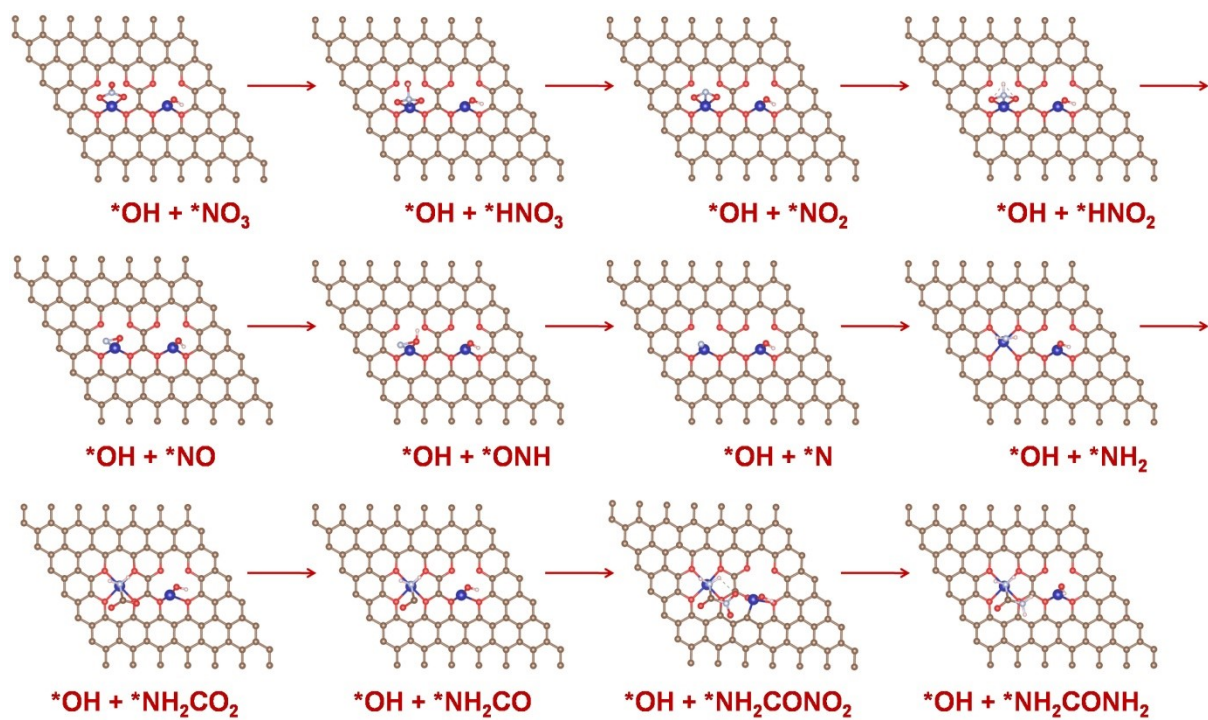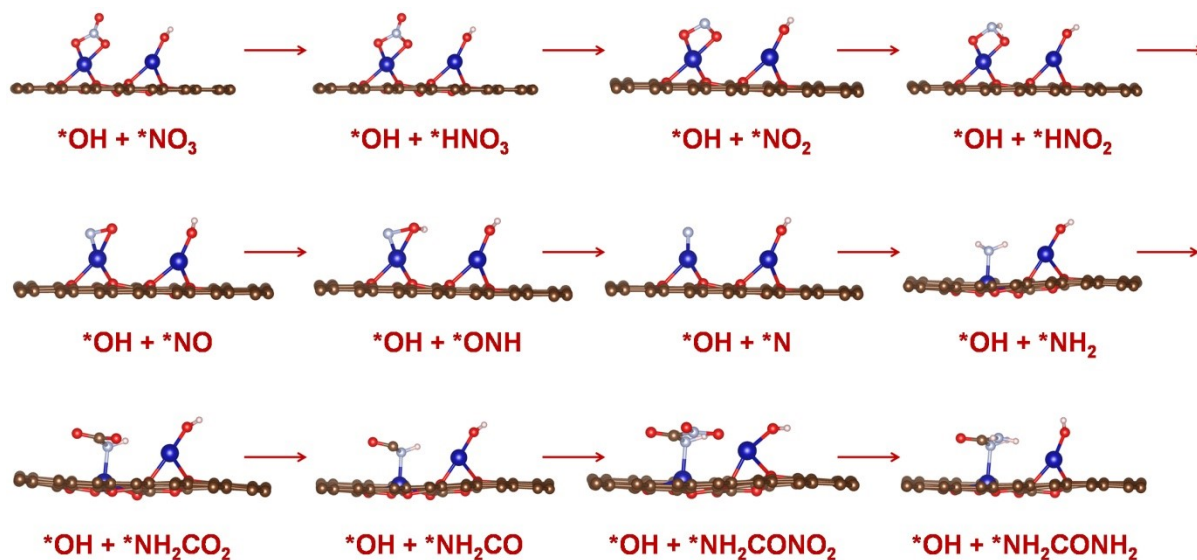
*NH$_2$ has higher nucleophility compared to *NO$_2$, therefore *NH$_2$ coupling with *CONH$_2$ should have higher probability, we simultaneously adsorb *CONH$_2$ and *NH$_2$ on each Co-(O-C$_2$)$_4$ site without considering the adsorption of *OH in alkaline electrolyte (*CONH$_2$ + *NH$_2$ → *NH$_2$CO$_2$NH$_2$ + *) (Fig. S41). The calculations results indicated that the corresponding kinetic energy barrier was calculated to be a large kinetic energy barrier of +1.11 eV for the formation of *NH$_2$CONH$_2$ on Co-(O-C$_2$)$_4$ site, which was much higher than *OH + *NH$_2$CONO$_2$ to *OH + *NH$_2$CONH$_2$ (−3.71 eV) (Fig. 5c). Therefore the process from *OH + *NH$_2$CONO$_2$ to *OH + *NH$_2$CONH$_2$ is more thermodynamically favourable for C−N coupling reaction.

Fig. S42. Corresponding intermediates structures of *OOH and *OH + *OOH. The blue, red, grey and white balls represent Co, O, C and H atoms, respectively.
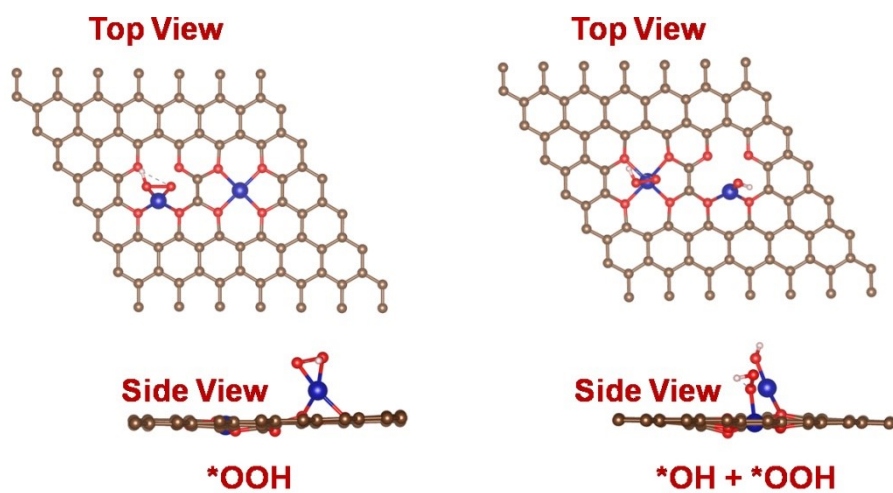
References

1   X. Wei, X. Wen, Y. Liu, C. Chen, C. Xie, D. Wang, M. Qiu, N. He, P. Zhou, W. Chen, J. Cheng, H. Lin, J. Jia, X.-Z. Fu and S. Wang, *J. Am. Chem. Soc.*, 2022, 144, 11530-11535.

2   S. Zhang, J. Geng, Z. Zhao, M. Jin, W. Li, Y. Ye, K. Li, G. Wang, Y. Zhang, H. Yin, H. Zhang and H. Zhao, *EES Catal.*, 2023, 1, 45-53.

3   K. Zhang, Y. Guo, Q. Ji, A.-Y. Lu, C. Su, H. Wang, A. A. Puretzky, D. B. Geohegan, X. Qian, S. Fang, E. Kaxiras, J. Kong and S. Huang, *J. Am. Chem. Soc.*, 2020, 142, 17499-17507.

4   K.-H. Jin, S.-M. Choi and S.-H. Jhi, *Phys. Rev. B*, 2010, 82, 033414.

5   S. Grimme, *J. Comput. Chem.*, 2006, 27, 1787-1799.

6   J. K. Nørskov, J. Rossmeisl, A. Logadottir, L. Lindqvist, J. R. Kitchin, T. Bligaard and H. Jónsson, *J. Phys. Chem. B*, 2004, 108, 17886-17892.

7   C. Chen, X. Zhu, X. Wen, Y. Zhou, L. Zhou, H. Li, L. Tao, Q. Li, S. Du, T. Liu, D. Yan, C. Xie, Y. Zou, Y. Wang, R. Chen, J. Huo, Y. Li, J. Cheng, H. Su, X. Zhao, W. Cheng, Q. Liu, H. Lin, J. Luo, J. Chen, M. Dong, K. Cheng, C. Li and S. Wang, *Nat. Chem.*, 2020, 12, 717-724.

8   D. B. Kayan and F. Köleli, *Appl. Catal. B: Environ.*, 2016, 181, 88-93.

9   M. Yuan, J. Chen, Y. Bai, Z. Liu, J. Zhang, T. Zhao, Q. Wang, S. Li, H. He and G. Zhang, *Angew. Chem., Int. Ed.*, 2021, 60, 10910-10918.

10   M. Yuan, J. Chen, Y. Bai, Z. Liu, J. Zhang, T. Zhao, Q. Shi, S. Li, X. Wang and G. Zhang, *Chem. Sci.*, 2021, 12, 6048-6058.

11   M. Yuan, J. Chen, Y. Xu, R. Liu, T. Zhao, J. Zhang, Z. Ren, Z. Liu, C. Streb, H. He, C. Yang, S. Zhang and G. Zhang, *Energy Environ. Sci.*, 2021, 14, 6605-6615.

12   M. Yuan, J. Chen, H. Zhang, Q. Li, L. Zhou, C. Yang, R. Liu, Z. Liu, S. Zhang and G. Zhang, *Energy Environ. Sci.*, 2022, 15, 2084-2095.

13   M. Yuan, H. Zhang, Y. Xu, R. Liu, R. Wang, T. Zhao, J. Zhang, Z. Liu, H. He, C. Yang, S. Zhang and G. Zhang, *Chem Catal.*, 2022, 2, 309-3207.

14   L. Pan, J. Wang, F. Lu, Q. Liu, Y. Gao, Y. Wang, J. Jiang, C. Sun, J. Wang and X. Wang, *Angew. Chem., Int. Ed.*, 2023, 62, e202216835.

15   X. Zhang, X. Zhu, S. Bo, C. Chen, K. Cheng, J. Zheng, S. Li, X. Tu, W. Chen, C. Xie, X. Wei, D. Wang, Y. Liu, P. Chen, S. P. Jiang, Y. Li, Q. Liu, C. Li and S. Wang, *Angew. Chem., Int. Ed.*, 2023, 62, e202305447.

16   Z. Lv, S. Zhou, L. Zhao, Z. Liu, J. Liu, W. Xu, L. Wang and J. Lai, *Adv. Energy Mater.*, 2023, 13, 2300946.

17   X. Chen, S. Lv, J. Kang, Z. Wang, T. Guo, Y. Wang, G. Teobaldi, L.-M. Liu and L. Guo, *Proc. Natl. Sci. U.S.A.*, 2023, 120, e2306841120.

18   D. Jiao, Y. Dong, X. Cui, Q. Cai, C. R. Cabrera, J. Zhao and Z. Chen, *J. Mater. Chem. A*, 2023, 11, 232-240.

19   M. Shibata and N. Furuya, *J. Electroanal. Chem.*, 2001, 507, 177-184.

20   P. Siva, P. Prabu, M. Selvam, S. Karthik and V. Rajendran, *Ionics*, 2017, 23, 1871-1878.

21   N. Cao, Y. Quan, A. Guan, C. Yang, Y. Ji, L. Zhang and G. Zheng, *J. Colloid Interf. Sci.*, 2020, 577, 109-114.

22   Y. Feng, H. Yang, Y. Zhang, X. Huang, L. Li, T. Cheng and Q. Shao, *Nano Lett.*, 2020, 20, 8282-8289.

23   S. Liu, S. Yin, Z. Wang, Y. Xu, X. Li, L. Wang and H. Wang, *Cell Rep. Phys. Sci.*, 2022, 3, 100869.

24   N. Meng, Y. Huang, Y. Liu, Y. Yu and B. Zhang, *Cell Rep. Phys. Sci.*, 2021, 2, 100378.

25   D. Zhang, Y. Xue, X. Zheng, C. Zhang and Y. Li, *Natl. Sci. Rev.*, 2023, 10, nwac209.

26   Y. Huang, R. Yang, C. Wang, N. Meng, Y. Shi, Y. Yu and B. Zhang, *ACS Energy Lett.*, 2022, 7, 284-291.

27   M. Shibata, K. Yoshida and N. Furuya, *J. Electroanal. Chem.*, 1995, 387, 143-145.

28   D. Saravanakumar, J. Song, S. Lee, N. H. Hur and W. Shin, *ChemSusChem*, 2017, 10, 3999-4003.

29   C. Lv, C. Lee, L. Zhong, H. Liu, J. Liu, L. Yang, C. Yan, W. Yu, H. H. Hng, Z. Qi, L. Song, S. Li, K. P. Loh, Q. Yan and G. Yu, *ACS Nano*, 2022, 16, 8213-8222.

30   C. Lv, L. Zhong, H. Liu, Z. Fang, C. Yan, M. Chen, Y. Kong, C. Lee, D. Liu and S. Li, *Nat. Sustain.*, 2021, 4, 868-876.

31   N. Meng, X. Ma, C. Wang, Y. Wang, R. Yang, J. Shao, Y. Huang, Y. Xu, B. Zhang and Y. Yu, *ACS Nano*, 2022, 16, 9095-9104.

32   J. Leverett, T. Tran-Phu, J. A. Yuwono, P. Kumar, C. Kim, Q. Zhai, C. Han, J. Qu, J. Cairney, A. N. Simonov, R. K. Hocking, L. Dai, R. Daiyan and R. Amal, *Adv. Energy Mater.*, 2022, 12, 2201500.

33   X. Liu, P. V. Kumar, Q. Chen, L. Zhao, F. Ye, X. Ma, D. Liu, X. Chen, L. Dai and C. Hu, *Appl. Catal. B: Environ.*, 2022, 316, 121618.

34   J. Qin, N. Liu, L. Chen, K. Wu, Q. Zhao, B. Liu and Z. Ye, *ACS Sustainable Chem. Eng.*, 2022, 10, 15869-15875.

35   X. Zhang, X. Zhu, S. Bo, C. Chen, M. Qiu, X. Wei, N. He, C. Xie, W. Chen and J. Zheng, *Nat. Commun.*, 2022, 13, 1.

36   J. Geng, S. Ji, M. Jin, C. Zhang, M. Xu, G. Wang, C. Liang and H. Zhang, *Angew. Chem., Int. Ed.*, 2023, 62, e202210958.

37   X. Wei, Y. Liu, X. Zhu, S. Bo, L. Xiao, C. Chen, T. T. T. Nga, Y. He, M. Qiu, C. Xie, D. Wang, Q. Liu, F. Dong, C.-L. Dong, X.-Z. Fu and S. Wang, *Adv. Mater.*, 2023, 35, 2300020.

38   N. Li, H. Gao, Z. Liu, Q. Zhi, B. Li, L. Gong, B. Chen, T. Yang, K. Wang, P. Jin and J. Jiang, *Sci. China Chem.*, 2023, 66, 1417-1424.

39   Q. Zhao, X. Lu, Y. Wang, S. Zhu, Y. Liu, F. Xiao, S. X. Dou, W.-H. Lai and M. Shao, *Angew. Chem., Int. Ed.*, 2023, 62, e202307123.

40   Y. Liu, X. Tu, X. Wei, D. Wang, X. Zhang, W. Chen, C. Chen and S. Wang, *Angew. Chem., Int. Ed.*, 2023, 62, e202300387.

41   M. Sun, G. Wu, J. Jiang, Y. Yang, A. Du, L. Dai, X. Mao and Q. Qin, *Angew. Chem., Int. Ed.*, 2023, 62, e202301957.

42   M. Qiu, X. Zhu, S. Bo, K. Cheng, N. He, K. Gu, D. Song, C. Chen, X. Wei, D. Wang, Y. Liu, S. Li, X. Tu, Y. Li, Q. Liu, C. Li and S. Wang, *CCS Chem.*, 2023, 0, 1-11.

43   S. Shin, S. Sultan, Z.-X. Chen, H. Lee, H. Choi, T.-U. Wi, C. Park, T. Kim, C. Lee, J. Jeong, H. Shin, T.-H. Kim, H. Ju, H. C. Yoon, H.-K. Song, H.-W. Lee, M.-J. Cheng and Y. Kwon, *Energy Environ. Sci.*, 2023, 16, 2003-2013.

44   Y. Wang, S. Xia, J. Zhang, Z. Li, R. Cai, C. Yu, Y. Zhang, J. Wu and Y. Wu, *ACS Energy Lett.*, 2023, 8, 3373-3380.

45   Y. Zhao, Y. Ding, W. Li, C. Liu, Y. Li, Z. Zhao, Y. Shan, F. Li, L. Sun and F. Li, *Nat. Commun.*, 2023, 14, 4491.

46   C. Chen, S. Li, X. Zhu, S. Bo, K. Cheng, N. He, M. Qiu, C. Xie, D. Song, Y. Liu, W. Chen, Y. Li, Q. Liu, C. Li and S. Wang, *Carbon Energy*, 2023, 5, e345.

47   Y. Luo, K. Xie, P. Ou, C. Lavallais, T. Peng, Z. Chen, Z. Zhang, N. Wang, X.-Y. Li, I. Grigioni, B. Liu, D. Sinton, J. B. Dunn and E. H. Sargent, *Nat. Catal.*, 2023, 6, 939-948.

48   D. Anastasiadou, B. Ligt, Y. He, R. C. J. van de Poll, J. F. M. Simons and M. C. Figueiredo, *Commun. Chem.*, 2023, 6, 199.